Chapter 9

SAR Oil Spill Imaging, Interpretation and Information Retrieval Techniques

Camilla Brekke[1] and Cathleen E. Jones[2]

Oil spills in the ocean reduce the small-scale surface roughness, leading to increased forward scattering and reduced backscatter (Figure 1.1).

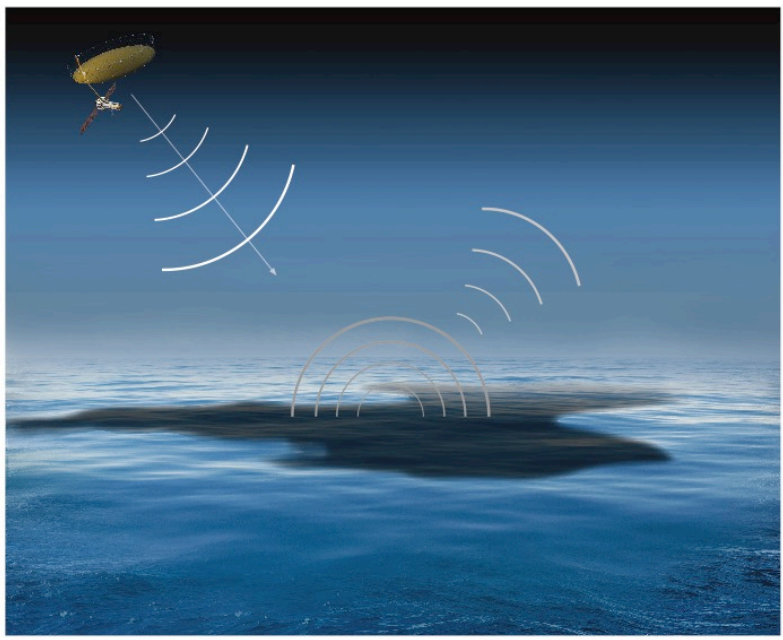

Figure 1.1 An oil spill causes increased forward scattering and reduced backscattering of the electromagnetic signal relative to nearby slick-free seawater.

This causes a slick to be darker than surrounding clean water in radar images and,

[1] UiT The Arctic University of Norway, Tromsø, Norway
[2] Jet Propulsion Laboratory, California Institute of Technology

conversely, brighter in optical images given suitable sunglint conditions. Environmental monitoring of vast ocean areas to identify accidental or intentional spills is a challenging and costly task, especially in Arctic regions that lack sunlight during the polar night and commonly experience harsh weather conditions. Remote sensing by synthetic aperture radar (SAR) is a key solution to this problem, allowing imaging of the sea surface independent of sunlight and cloud coverage. SAR-based marine petroleum hydrocarbon spill (hereinafter referred to as *oil spill*) monitoring services support two main needs for information. First, regular surveillance of the seas is needed to detect the presence of accidental and illegal man-made oil spills. Second, during oil spill response operations, authorities need to know the characteristics of the spill, such as its extent, a forecast of how it will spread and be transported in the marine environment, and the location of the combatable thicker oil within the slick.

This chapter addresses the physical mechanisms behind SAR imaging of oil spills in the open ocean and proceeds with a discussion on the emerging SAR information retrieval techniques for detecting and characterizing these slicks. Section 1.1 covers oil spill information items possibly derived from SAR and limitations of existing methods. Challenges and trade-offs faced by operational service providers in retrieving these items are discussed in Section 1.2. Section 1.3 is about SAR image interpretation: the main contrast drivers for oil spills are explained and surface scattering models aiding interpretation are reviewed. In section 1.4, the main techniques for oil spill detection and characterization are illustrated and current research questions are discussed. Concluding remarks and notes on further readings are given in section 1.5.

1.1 Information items requested and gaps

According to [1], there are six general oil spill-specific applications of remotely sensed data from any sensor: surveillance and detection, mapping for both tactical (short term) and strategic (long term) countermeasures, trajectory determination, direct support for oil spill countermeasures, gathering of legal evidence, and law enforcement regarding ship discharge of pollutants.

Table 1.1 summarizes some of the key information items available either directly or indirectly from SAR measurements. The phase of oil spill operations at which the information is needed is indicated. In practice there is a large degree of latitude in acceptable latency depending on the specific situation because spills evolve differently depending on the meteorological and sea surface (metocean) conditions.

Current satellite SAR oil spill services aim to provide near real-time delivery of information after a scene is acquired and downlinked. For example, the European Maritime Safety Agency (EMSA) requires maximum delivery times of 20-120 minutes depending on the product (per Invitation to Tender No. EMSA/OP/6/2018), although specific operations depend upon the service organization, their access to satellite imagery, and the geographical location of the satellite downlink ground station. EMSA has a central role in monitoring and preventing pollution in European Union seas and ports. The agency uses satellite-based oil spill information from CleanSeaNet (CSN) to assist ship-source pollution response, as described for the North Sea region during 2007-2011 in [2]. During this period, three SAR satellites

were used (ENVISAT, Radarsat-1 and -2) to cover 1000 million km^2 sea area and 8666 possible spills were detected. Out of these, 2828 were checked on site, and 50% within 3 hours by aerial surveillance. Of the confirmed releases (745), 80% were mineral oil and 20% other substances. These statistics reveal one potential problem with the operational slick detection methodology: although rapid detection is important in the early warning phase, false alarms are a major concern. Even though satellite SAR provides a valuable synoptic overview of large ocean areas, natural slicks can trigger expensive aircraft or vessel operations. For comparison, the U.S. National Oceanic and Atmospheric Administration Satellite and Information Service (NOAA NESDIS) prepares Marine Pollution Surveillance Reports (MPSRs) [3] based on semi-automated surveys of remote sensing data by operational analysts. Potential releases are checked against the locations of known seeps, pipelines, rigs, well heads, and ship wrecks and local metocean conditions from buoys or models before reports are filed. Analysts use all available optical and SAR imagery, with Sentinel-1 now the dominant source. The latency between image acquisition and report submission ranges from 2 hours to >24 hours in exceptional cases, with typical delay of 8 hours for Sentinel-1 scenes [Ellen Ramirez, private communication]. Between 200 and 300 reports are generated per year and human intervention in the image screening process eliminates many false alarms. In principle the combination of latency and false alarms could be reduced through automation but currently there is no robust method to automatically differentiate accidental or intentional mineral oil spills from natural slicks using SAR. There is only an indication of SAR-based determination of relative difference between oil spill types (mineral vs. biogenic) reported in the literature [4] (also see section 1.4.2). This is an outstanding knowledge gap between information needed by the authorities and other stakeholders and the information provided through satellite SAR alone.

During the tactical clean-up stage of a major oil spill combat situation, responders need to know the location of thicker layers of oil in the surface slick to initiate clean-up procedures such as in situ burning and mechanical or chemical dispersal or recovery [5]. A sea surface oil spill is spatially nonuniform and typical contains zones of thicker and thinner oil layers, whether the oil is emulsified or not. It is established practice to separate areas within the slick between five distinct categories based on the visual appearance of the slick following the Bonn Agreement for Oil Appearance Code (BAOAC) [6]. The categories correspond to order-of-magnitude ranges of thickness and volume of the oil (see Table 1.2) and the classification is typically done by experienced observers from low-flying aircraft. Emulsions, which are mixtures of oil and water, increase the viscosity, volume, and thickness of the material and can be very stable [7].

A comparable SAR-based system to quantify thickness currently does not exist and its development is complicated by several factors. First, SAR does not measure the thickness directly, so a physical model must be developed relating how oil layer thickness affects the parameters that influence the backscatter of waves in the microwave region of the electromagnetic spectrum. The main parameters are the ocean wave spectra and the dielectric constant. In the case of the latter, emulsification of the oil, i.e., the creation of stable or meta-stable oil-in-water or water-in-oil mixtures with altered dielectric properties from oil or seawater, is indirectly related to thickness because some forms of emulsions clump to form thick layers. Second, the small-scale ocean surface roughness is strongly influenced by

instantaneous wind conditions and the large-scale wave structure depends on wind history and background swell. A valid model must account for these effects. The last complicating factor is a limitation of SAR instruments, namely a requirement that the SAR be sensitive to sufficiently low levels of backscatter to measure thickness variation. Because the backscatter intensity decreases as the thickness increases or dielectric constant decreases [8], instrument noise can dominate the measured signal over a slick, preventing accurate determination of thickness for the thicker oil layers.

Table 1.1 Key information items pertaining to oil spill surveillance, response, remediation, and preparedness involving SAR.

Use	Information item	Comment
Detection & early warning	Position	Latitude/longitude information obtainable from SAR directly.
	Source of origin	Oil spill source and trajectory prediction (hindcasting) models can be initialized by slick position in SAR.
	Drift estimate (surface velocity)	Requires consecutive SAR acquisitions within minutes to hours to allow spatial feature correlation (nowcasting).
	Extent	Surface areal extent obtainable from SAR directly.
	Slick type discrimination*	Only relative difference between oil slick types** (no label) obtainable from SAR.
Tactical clean-up stage	Volumetric oil fraction*	Estimated directly from SAR for thick slicks, but requires assumptions on the dielectric constants of crude oil and sea water.
	Thickness*	Only zones of relative larger thickness obtainable from SAR. Absolute thickness determination* requires calibration.
Tactical clean-up stage and long-range monitoring	3-D drift and spread prediction (surface velocity and vertical entrainment)	Numerical (forecasting) models can be initialized by slick contours provided from SAR.
Strategic planning: Environmental impact analysis	Oil trajectory statistics	Numerical (forecasting) models can be initialized by slick contours provided from SAR and run for different metocean conditions.
Strategic planning: Statistics of spill occurrence	Mapping	Position and contour obtainable from SAR.
Remediation: Legal evidence	Volume*	Estimate from extent and thickness. Requires some calibration of SAR-derived relative thickness and modelling to estimate the entrained volume.

*More studies are needed on this topic. **Mineral vs. biogenic oil slicks.

Nonetheless, the potential of SAR for measuring relative thickness [9] or the volumetric oil fraction of emulsified oil [10,11] has been demonstrated. With calibration using field observations of slick thickness, the SAR backscatter can be related to absolute thickness for a given slick and metocean conditions [12]. A relation between the BAOAC and a proposed oil/water mixing index (Mdex) to

separate sheen from emulsions is proposed in [13]. Oil spill characterization is discussed further in section 1.4.2.

The aim of oil spill modelling is to describe the slick's transport and fate in open seas. Upon initial detection, there is immediate need for information on the oil spill source location, and both tactical and strategic planning relies on reliable predictions of the oil slick's future location. Therefore, both hindcasting and forecasting of the trajectory are important and, arguably, determining the source of origin can be more important in some situations. The drift velocity can be derived from two or more SAR images alone by feature correlation, but due to the time lag between two satellite SAR acquisitions, the speed is underestimated when the movement is not linear and the spatial shape of the spill, input to feature tracking, may not be recognizable if the lag is too long, hampering this method. Due to the limitation on the revisit time of space-borne SARs (discussed in section 1.2.2), source identification by SAR is usually not reliable. The slick position and extent can be extracted from space-borne, air-borne, or ship-borne radar and used as input to oil spill hindcast trajectory models [14] or forecast models to predict the future trajectory. Oil on the ocean surface elongates in the direction of the wind while horizontal transport of oil droplets entrained in the water column is to a large extent determined by the currents. A reliable quantitative measure of slick volume cannot be derived from SAR images alone as the slick evolves because detection of oil particles within the water column is impossible due to the high conductivity of sea water. However, information about particle entrainment into the water column can be obtained by combining SAR and numerical models. Forecasting surface velocity and vertical particle entrainment is addressed in section 1.4.3.

Table 1.2 Oil classes and the corresponding thickness and volume ranges from the BAOAC [6]. Emulsified oil or 'mousse' are oil-water mixtures that can be considerably thicker than a few millimetres and are characterized by color in shades of orange, brown, and/or red [7].

Code	Appearance Description	Layer Thickness (μm)	Layer Volume (liter/km^2)
1	Sheen (silvery/grey)	0.04 – 0.30	40 – 300
2	Rainbow	0.30 – 5.0	300 – 5000
3	Metallic	5.0 – 50	5000 – 50 000
4	Discontinuous true color	50 – 200	50 000 – 200 000
5	Continuous true color	≥ 200	≥ 200 000

In general, it is clear that oil spill response requires rapid imaging and processing because slicks can move and change quickly on the sea surface, and that the longer the revisit time of the satellite missions, the less efficient satellite-based SAR approaches will be. Airborne SAR can provide very rapid repeat imaging to track the trajectory and fate of oil slicks [9] to support response and remediation, but would still rely upon satellite surveillance programs for initial detection. Airborne SAR has an advantage over spaceborne SAR in characterizing the oil thickness or volume because of the higher instrument signal-to-noise ratio (SNR) (discussed in section 1.3.3).

1.2 Challenges

Vast ocean areas must be monitored continually by operational services to identify potential oil spills. Retrieving the information items discussed above involves several challenges and trade-offs that relate to factors both intrinsic and extrinsic to the methods and remote sensing instruments employed. The feasibility of executing oil spill clean-up operations depends to a large degree on the weather conditions, solar illumination, geography such as local topographic features that potentially influence wind fields and navigability, and tactical deployment issues like the local settlement and infrastructure and the accessibility of the polluted region [15]. SAR sensors operate at different frequencies and different polarizations, with a choice of operational modes that in some cases trade spatial resolution for image areal coverage. Oil slicks move with wind and currents and the physical and chemical properties evolve with time, changing not only their persistence and environmental impact, but also their characteristic signatures for remote sensing. The major challenges that relate to the use of SAR for oil spill response are discussed in this section.

1.2.1 Polarization diversity

SAR antennas are designed to transmit and receive linearly polarized electromagnetic waves, with the orthogonal orientations denoted 'vertical' (V) and 'horizontal' (H). Circular polarization can be synthesized by simultaneously transmitting H and V pulses 90° out of phase in the time domain. Single-polarization (SP) systems transmit and receive the same polarization; dual-polarization (DP) systems transmit one polarization and can receive both the same and the orthogonal polarization; and quad-polarization (QP) systems transmit and receive two orthogonal polarizations. Electromagnetic scattering can be completely characterized by QP systems. Co-polarized returns have the same transmit and receive polarization (e.g., HH or VV, where the first (second) letter indicates the transmit (receive) polarization), and cross polarized returns have orthogonal transmit and receive orientations (e.g., HV or VH). In rare cases, a DP product will be available with the two co-polarized returns (HH and VV), but typically DP modes are either horizonal (HH and HV) or vertical (VV and VH). A polarimetric system preserves and records the relative phase between and among the transmit and receive pulses, and systems that do not do this are called 'incoherent.' The term 'compact polarization' (CP) refers to systems that do not maintain the DP collinear/orthogonal convention of the transmit and receive channels, and hybrid polarization (HP) [16] is one particular variant in which circular polarization is transmitted and linear polarization received. HP systems typically are not QP, i.e., they transmit only right or only left circularly polarized waves.

SAR-based oil spill detection services have traditionally relied on single- and dual-polarization SAR systems with large spatial coverage. Over the last decade or so, several quad-polarimetric (QP) SAR systems have been launched into orbit, with Radarsat-2 (Canadian) launched in 2007 and Gaofen-3 (Chinese) in 2016. QP SAR allows improved interpretability and information retrieval regarding the polarization-dependent properties of a scattering surface, however the increased information content usually comes at the cost of reduced spatial coverage. For

example, Radarsat-2 Fine QP mode covers a 25 km swath [17], whereas Sentinel-1 extra wide (EW) SP and DP modes have 410 km swath width. Compact polarimetry was introduced to allow simultaneously high spatial coverage and increased polarimetric content [18], although compact polarimetry SAR still falls between conventional dual-polarization and quad-polarimetric SAR systems in terms of polarimetric information. The HP mode [16] has already been integrated into several missions, e.g., RISAT-1 (Indian), ALOS-2 (Japanese), and the Radarsat Constellation Mission (RCM) (Canadian). High spatial resolution is not needed in many cases for oil spill monitoring. However, it can be useful for nowcasting of the drift using pixel offset tracking, for locating a point source on the surface like a rig or ship, for identification of internal slick zones, and for false alarm discrimination when the slick's shape or other spatial characteristics are used to differentiate natural phenomena from spills.

Table 1.3 Parameters of civilian SAR instruments operating currently, in the recent past, or under development. The 'Remarks' contain information about polarization modes of particular relevance to oil spill surveillance. RISAT-1 deactivated in 2016. [FQ: Fine Quad. SM: Stripmap. LN: Low Noise. PP: PingPong. EW: Extra Wide-swath mode.] [Polarization modes: HH: H-transmit, H-receive. VV: V-transmit, V-receive. QP: Quad-polarimetry. HP: Hybrid Polarity (Circular-transmit, Linear-receive). DP: Dual-polarimetry. QQP:Quasi-quad-polarimetry (DP HH/HV and DP VV/VH)].

Band	Mission	Launch (year)	NESZ (mode/ channel)	Repeat (day)	Remarks
X	TerraSAR-X [20]	2007	-19 dB (SM)	11	DP HH/VV*
	COSMO-Skymed 1-4 [21,22]	2007-2010	-22 dB	1-8**	PP HH/VV (incoherent)
C	Radarsat-2 [17]	2007	-39 to -31 dB (QP)	24	QP
	RISAT-1 [23]	2012	-17 dB (FRS-1)	25	HP
	RCM [24]	2019 (plan)	-25 dB (LN)	4***	HP
	Sentinel 1A/B	2014/2016	-22 dB (EW)	6+	EW
	Gaofen-3 [25]	2016	-33 dB (QP++)	29	QP
L	ALOS-2 [26]	2014	-36 dB (SM++)	14	QP
	SAOCOM 1A/B [27]	2018 1A, 2019 1B (plan)	-35 dB (SM)	8+	HP
	NISAR	2022 (plan)	-25 dB%	12	QQP

* The dual-co-polarization combination of HH/VV is preferred for oil spill monitoring [19]. ** For constellation of four satellites. *** For constellation of three satellites. + For constellation of two satellites. ++ For HH channel. % NISAR's requirement is that the NESZ be less than -25 dB across the full spectrum. Actual average value will be known after the hardware is built and will vary by mode.

Table 1.3 gives some relevant operating parameters of current, recent past, and near-term future SAR instruments. Almost all provide SP or DP products, so the table includes information about other oil-spill relevant modes available as standard products. The table also includes the levels of noise equivalent sigma zero (NESZ) for comparison across the different missions and modes, and to inform further

discussions in section 1.3.3. The upcoming L-band NASA-ISRO SAR (NISAR) (USA/India collaboration) mission is designed with a new polarimetric mode specifically for ocean studies, called quasi-quad-polarimetry (QQP). NISAR will be able to operate with an 80 MHz bandwidth in its highest resolution mode, but more generally will acquire data at 20 MHz bandwidth to reduce the data volume. The QQP mode splits the full spectrum to obtain simultaneously-acquired HH/HV and VV/VH DP modes. One polarization will be transmitted with 20 MHz bandwidth in the lower half of the spectrum and the other with 5 MHz bandwidth in the upper half. This allows the preferred HH/VV combination to be exploited for oil spill observations, but at disjoint frequencies. The small shift in frequency will have little impact on ocean studies, most of which do not require coherent VV and HH data. The use and usefulness of polarization in oil spill studies will be discussed in sections 1.3 and 1.4, respectively.

1.2.2 Imaging repeat interval

SAR satellites are usually launched in a polar orbit and image the ground with a fixed swath width that is mode-dependent. The satellite *repeat cycle* is the exact repetition of acquisition over the same location with the same imaging geometry. However, many locations can be imaged from different orbits because the spacing between the orbit tracks varies with latitude, and hence the revisit rate for imaging irrespective of geometry is much better at higher latitudes. The *temporal resolution* of a satellite is here defined as the time lag between two possible image acquisitions of the same area, either fully or partly overlapping and irrespective of imaging geometry. Table 1.3 shows the satellites' repeat cycle and Figure 1.2 illustrates the significant drift and evolution of the shape of various oil spills between two consecutive SAR acquisitions by Radarsat-2. The images were acquired 11.5 hours apart in FQ mode and the radiometric changes are dominated by the difference in imaging geometry. Given the number of currently operational space-borne SAR missions (Table 1.3), higher temporal resolution is obtained when multiple sensors are exploited. However, uniform and consistent analysis across the different systems requires a thorough understanding of the differences between the various sensors and modes [18] and of the incidence angle-dependence and wind-dependence of the backscatter.

Airborne SAR instruments can reimage a slick from the same viewing geometry much more rapidly than satellite SARs, typically several times per hour. Figure 1.3 shows an example of a mineral oil seep imaged with the Uninhabited Aerial Vehicle Synthetic Aperture Radar (UAVSAR) L-band instrument six times in 2 hours. The selected scenes shown are obtained 71 minutes apart. In this case, besides transport and spreading, the time evolution of the radiometry can provide information on weathering processes. With time series data it is possible to measure transport of the thicker oil within the slick using the intensity as a proxy for thickness (darker returns in areas of relatively thicker or more emulsified oil).

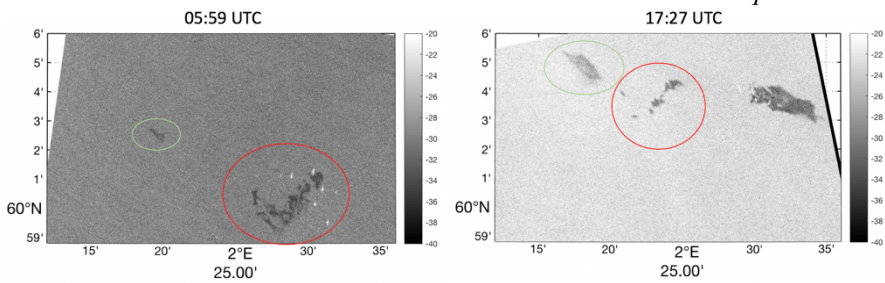

Figure 1.2 RADARSAT-2 VV intensity [dB] from two consecutive images of the same oil spills, showing both drift and change in size and shape of the slicks over an 11.5 hour period. The increase in intensity from unslicked seawater arises from the change in incidence angle. Circled in green: plant oil spill. Circled in red: emulsion oil spill. Not circled in image on right: crude oil spill. RADARSAT-2 Data and Products Copyright MDA LTD. (2011)—All rights reserved.

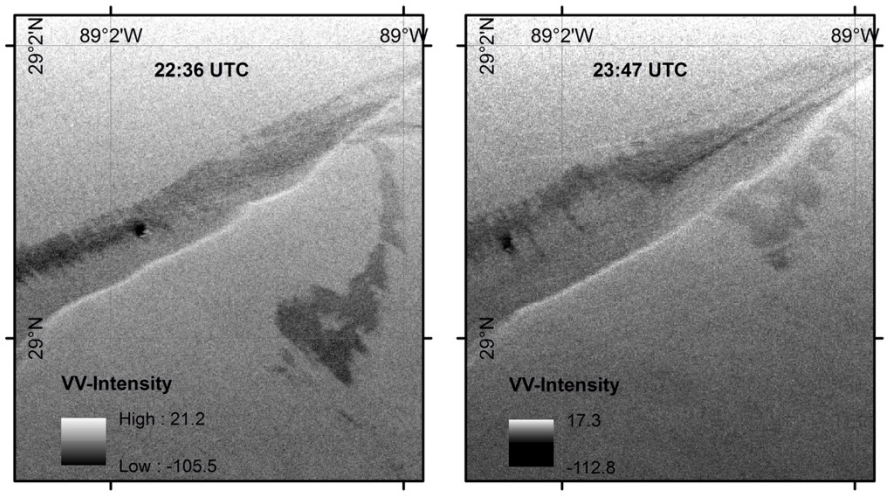

Figure 1.3 UAVSAR VV intensity [dB] from two images acquired 71 minutes apart of a slick originating from a seep. A mat of red-brown emulsion, identified visually from a low-flying aircraft and identifiable by the low radar return, is moving to the west-southwest.

1.2.3 The weather window

The weather window is defined here as the wind speed range over which SAR is usable for imaging oil spills, and is related to the sea surface geometry at the scale of the radar wavelength. Much effort has been devoted to relating the normalized radar cross section to near-surface wind speeds, either empirically based on power laws [28] or theoretically based on physical models [29]. Oil spill detection by SAR is generally confined to wind speeds in the range of 2-3 m/s to 10-14 m/s [30, and references therein], but the minimum wind speed to generate Bragg waves producing measurable radar returns varies with frequency. Some approximate thresholds at 20°

incidence angle are ~2.5 m/s for X-band, ~2.2 m/s for C-band and ~2.0 m/s for L-band [19,29]. These thresholds increase slightly with incidence angle and decrease with ocean temperature. At the high end of the range, the limit comes from mixing of the oil into the water column by breaking waves and the fact that the backscatter contrast between clean and slicked water decreases as the wind speed increases [31].

1.2.4 Transport and weathering of oil pollutants

After release, oil from spills at sea evolve through transport and weathering [32]. Slicks spread through the influence of gravity and winds, and are transported both on and below the sea surface. Oil released into the marine environment also develops over time through *weathering processes* acting on the pollutant and transforming its original physical and chemical properties. Some important transforming processes are evaporation, emulsification, dissolution, oxidation, and biodegradation [32], some of which act rapidly. These processes determine the fate of an oil spill in the marine environment and they have implications for response and combat procedures. In the context of a clean-up operation, and taking the time-dependent weathering processes into account, the amount and type of the pollutant, the sea state, and the prevailing environmental and weather conditions will determine which active countermeasures should be made. Hence, information obtained from SAR measurements benefit from rapid sampling and, if possible, resampling of the radar images to maintain its relevance during field operations. Examples of oil spill development with time were shown in Figure 1.2 and Figure 1.3, with examples from 'rapid' satellite SAR imaging (< 1/2 day) and much more rapid (~1 hour) airborne SAR repeat imaging performed in a single flight.

Table 1.4 Description of some selected processes affecting the fate of oil from a spill that depend on sea-state and oil properties.

Process	**Description**
Emulsification	Oil (immiscible) is dispersed by droplets of sea water. Contributes to the persistence of the spill due to an increase in viscosity and thickness with water content [33]. Stable emulsions contain 60-85% water [32].
Horizontal spreading	Spreading of oil on the sea surface mainly in early phases after release [32]. The spread is not necessarily uniform and observations have revealed that 90% of the oil can be confined to an area of less than 10% of the slick extent [34].
Vertical dispersion and entrainment	Movement of oil droplets (size < 100 μm [32]) into the water column. A rule of thumb for the depth of mixing during entrainment says 1.5 times the wave height [32]. Wave breaking is required to initiate entrainment of a surface spill. Diffusion can mix the oil deeper into the water column [35].

Table 1.4 gives a brief description of selected transport and weathering processes of particular relevance for this chapter. Geophysical parameters that can be affected by the presence of an oil slick on the ocean surface are the surface roughness, dielectric complex permittivity, surface tension, and surface viscosity. In sections 1.3 and 1.4, we discuss how emulsification of oil changes the dielectric

properties of the slick, which has an impact on its radar backscatter. In section 1.4.3, we exhibit how SAR imagery can be integrated with modelling for improved understanding of the horizontal spreading and vertical entrainment and mixing.

1.2.5 False alarms

The accuracy of both manual and automatic oil spill detection services is reduced due to the presence of *look-alikes*, i.e., other physical phenomena causing dark signatures in SAR imagery. There are a number of situations that give rise to radar-dark features in the ocean that are look-alikes for oil spills and can cause false alarms in SAR-based surveillance. To illustrate the difficulty, we compare mineral oil slicks with look-alikes on the sea surface. Figure 1.4 presents three examples of SAR scenes containing man-made oil slicks, which appear as dark spots on a brighter background. The left panel shows an example of a reoccurring produced water slick from an oil rig. Several examples of spilled emulsified oil are shown in the middle and right panels, and small plant oil spills (look-alikes) are visible in the upper right part of the middle panel and to the left of the large slick in the right panel. Examples of other look-alikes are low wind areas, grease ice, and natural biogenic films caused by, e.g., algae, fish oil, and vegetable oil. If the interest is exclusively in detecting man-made oil spills or seeps, natural oil seeps also fall into the look-alike category. Figure 1.5 shows examples of SAR images of algae bloom and low wind, both naturally occurring radar dark features. In Figure 1.6, grease ice is seen as dark slicks in the SAR scenes.

A variety of descriptors such as spatial, contextual, and statistical features are often used to label and discriminate the slicks [36]. Hence, it is obvious that the SAR sensor's spatial and radiometric resolutions, along with the instrument noise floor, are of importance for the mineral oil slick discrimination capability.

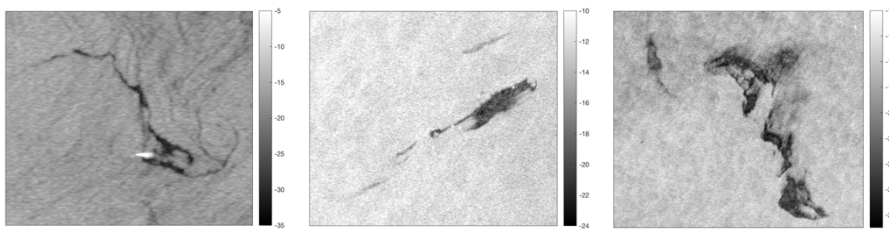

Figure 1.4 Examples of man-made oil spills. All scenes are from the North Sea. Intensity of VV polarization channel [dB], C-band. (Left) Produced water at the Brage oil production field. (Middle) Emulsion oil slicks from an oil-on-water exercise in 2013, with a small plant oil slick above the main emulsion slick. (Right) Oil slicks from an oil-on-water exercise in 2012. A small plant oil spill is located at upper left and emulsion slick is on the right. RADARSAT-2 Data and Products Copyright MDA LTD. (2017, 2013, 2012)—All rights reserved.

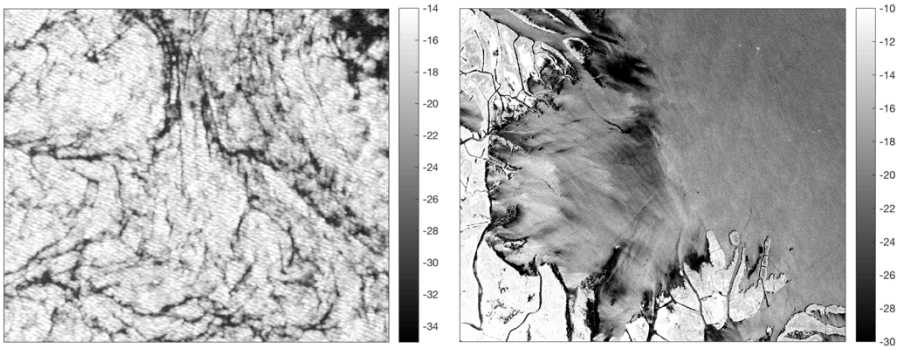

Figure 1.5 Examples of look-alikes. Intensity of VV polarization channel [dB]. (Left) RADARSAT-2 (C-band) scene of an algae bloom in the Baltic Sea. RADARSAT-2 Data and Products Copyright MDA LTD. (2016)—All rights reserved. (Right) UAVSAR (L-band) scene of low wind condition and calm water over subaqueous vegetation within islands in the Wax Lake Delta, Louisiana, USA.

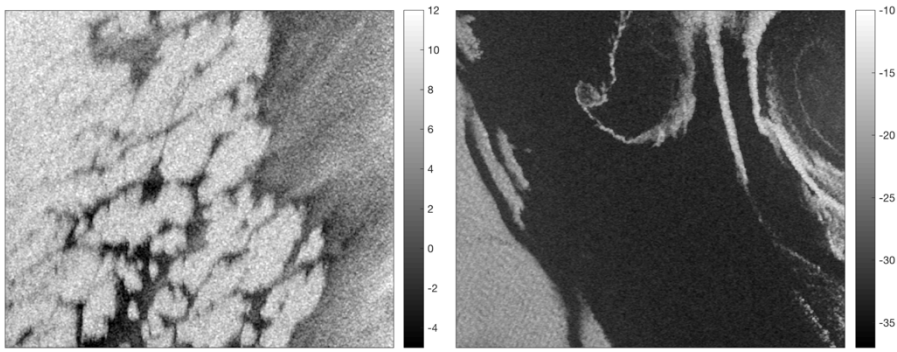

Figure 1.6 Examples of look-alikes. Intensity of VV polarization channel [dB], C-band. Both panels show newly frozen sea ice causing dark slicks. (Left) Open water and grease ice in the Barents Sea. Interpretation from comparing with timeseries of Sentinel-1 data. (Right) Grease ice along the ice margin near Hopen island. RADARSAT-2 Data and Products Copyright MDA LTD. (2017, 2014)—All rights reserved.

1.3 Interpretation and modelling

To explain the contrast between an oil spill and the ambient sea water in a SAR image, we introduce the properties that characterize a material and dictate the scattering of electromagnetic waves. Next, we revisit and discuss how surface scattering models may aid interpretation of real SAR measurements. Finally, we discuss the implications of the signal's proximity to the noise floor, which can be critical to interpretation of radar-dark signals.

1.3.1 Contrast drivers

In SAR imaging, there are two main drivers of contrast, i.e., a change in backscatter power, between an oil slick and the surrounding clean sea surface. One driver is the slick's capability of damping the small-scale roughness, causing a smaller portion of the reflected radar energy to be scattered back to the radar antenna. A second driver is the change in dielectric properties within an oil spill as compared to uncontaminated sea water. Both are discussed below.

1.3.1.1 Surface roughness

All of the SAR instruments listed in Table 1.3 are side-looking and operate in a monostatic configuration (transmitter and receiver collocated). Therefore, they measure the backscattered signal, which has larger amplitude for rougher surfaces. If the surface was perfectly smooth, the angular pattern of the reflected scatters would be a delta function centered on the specular direction, and the sensor would detect no backscatter. When the surface is slightly rough the angular radiation pattern has two components, the coherent scattering component, which is the reflection component in the specular direction, and the diffuse scattering component, which represents scattering in all directions. The coherent part becomes negligible when the roughness increases, and the radiation pattern approaches Lambertian scattering for very rough surfaces [37].

Two parameters are commonly used to characterize a naturally random surface: the spread of heights about the average value (vertical) and the variation of these heights across the surface (horizontal). The standard deviation of the surface height variation, σ_z, is referred to as the root mean square (rms) height of the surface. To model the smoothness of a surface, i.e., the correlation of the random height variations in the lateral direction, an idealized surface correlation function is typically used together with the correlation length, l [38]. For two points on the surface, the surface correlation describes their statistical independence and the correlation length increases with the distance between two correlated points (for a smooth surface $l = \infty$). Given a specific correlation function, the spatial roughness of a surface is fully described by the rms height, σ_z, and the surface correlation length, l [38]. The impact of surface roughness on radar backscatter depends strongly on the wavelength of the radar, λ_r. This is accounted by scaling the roughness parameters by the wavelength of the radar, yielding $k_r\sigma_z$ and $k_r l$, where $k_r = 2\pi/\lambda_r$ is the radar wavenumber [39].

The dominant contribution to radar backscatter is from Bragg resonance scattering, namely resonant scattering from spatially-correlated, wind-generated ocean wave components that are in phase with the incident radar waves. These components fall within the range from small capillary ripples to short gravity waves, depending on the radar frequency [19]. The Bragg wavelength of ocean waves resulting in resonance with the radar waves is given by $\lambda_B = n\lambda_r/(2\sin\theta)$, where θ is the incidence angle and $n = 1,2,\ldots$ is the order of resonance with $n = 1$ producing the dominant return. For a given λ_r, the resonant waves are shorter at more oblique θ, and at a given incidence angle λ_B increases with λ_r. In general, the Bragg scattering model is incomplete to describe the backscatter from the ocean surface because longer waves also interact with the Bragg waves and affect the radar return through tilt modulation (changing the local surface orientation or slope),

hydrodynamic modulation (changing the spatial distribution of ocean wave spectral components, e.g., as short waves pile up in crests and spread out in troughs), and velocity bunching (nonlinear modulation caused by the SAR processing, which translates the surface velocity component in the look direction into a position shift in azimuth direction due to the Doppler shift) [40,41].

1.3.1.2 Relative dielectric constant

The dielectric properties of the scattering surface affect the electromagnetic interaction between the electromagnetic wave and the surface, and hence the backscattered signal. The *relative permittivity*, ϵ_r, of a material is a complex number given by

$$\epsilon_r(\omega) = \big(\epsilon'(\omega) - i\epsilon''(\omega)\big)/\epsilon_0,$$

where $\epsilon'(\omega)$ is the real part of the material's permittivity, $\epsilon''(\omega)$ is the imaginary part, ϵ_0 is the vacuum permittivity (permittivity of free space), $i = \sqrt{-1}$, and $\omega = 2\pi\nu$ is the angular frequency (also referred to as radian frequency) of the incident radar wave with frequency, ν. The term *dielectric constant* has been used interchangeably with the electric permittivity and also to refer to the real part of the relative permittivity. The term *relative dielectric constant* is here used to describe the complex ϵ_r.

A reduction in the effective relative dielectric constant means less total energy being reflected by the surface, and hence, the surface will appear darker. As discussed in section 1.2.4, oil mixes with sea water through interaction with waves and weathering to form oil/water emulsification. Oil has a relative dielectric constant around $\epsilon_r^O = 2.3 - i0.02$ [10], much lower in both real and imaginary components than that of sea water, ϵ_r^{SW}, which is a function of temperature, T, and salinity, S, but exceeds ϵ_r^O under almost all open water ocean conditions. For example, calculations based on [37] for 1.26 GHz (L-band) frequency give $\epsilon_r^{SW} = 70.1 - i82.7$ for typical Gulf of Mexico conditions (T=27°C, S=35ppt) and $\epsilon_r^{SW} = 75.4 - i59.4$ for typical North Sea conditions (8°C, S=35.25ppt). Oil/water emulsions have relative dielectric constant lying between ϵ_r^O and ϵ_r^{SW}. Recent work at L-band has suggested that it is possible to quantify the mixing of oil and sea water from SAR, based on work using a simple linear mixing model for the emulsion relative dielectric constant [10,13] or the more accurate Bruggeman formula [11].

Figure 1.7 depicts the impact of oil mixing with sea water on the relative dielectric constant. Radar backscatter is only sensitive to the slick's dielectric properties if the backscatter occurs from the oil, not the underlying sea water interface. This is caused by a thick layer of oil or oil emulsion on the sea surface [10, 13]. Typically, most of a slick is not thick, with the general rule being that 90% of the oil is contained in 10% of the slick area [34]. Because of oil's low loss factor (imaginary part of ϵ_r^O), electromagnetic waves pass through very thin layers of oil without interacting, and so see an effective relative dielectric constant of sea water, same as for the clean water. This is certainly true for sheen layers (Table 1.2). Although studies have inferred the oil volumetric fraction from backscatter [10,11,13], none have yet been validated to determine the thickness threshold at which the oil layer's relative dielectric constant impacts backscatter. However, it is known that emulsions often form thicker layers [7] and observed that red-brown emulsions within slicks have much lower backscatter than the rest of the slick [9,42].

This is a topic of active study. Although it is known from electromagnetic scattering theory that the layer thickness for interaction must be comparable to the wavelength within the medium, determination of the thresholds for both thickness and oil volumetric fraction at which the backscatter becomes sensitive and experimental confirmation for an oil spill in the open ocean remains an outstanding issue.

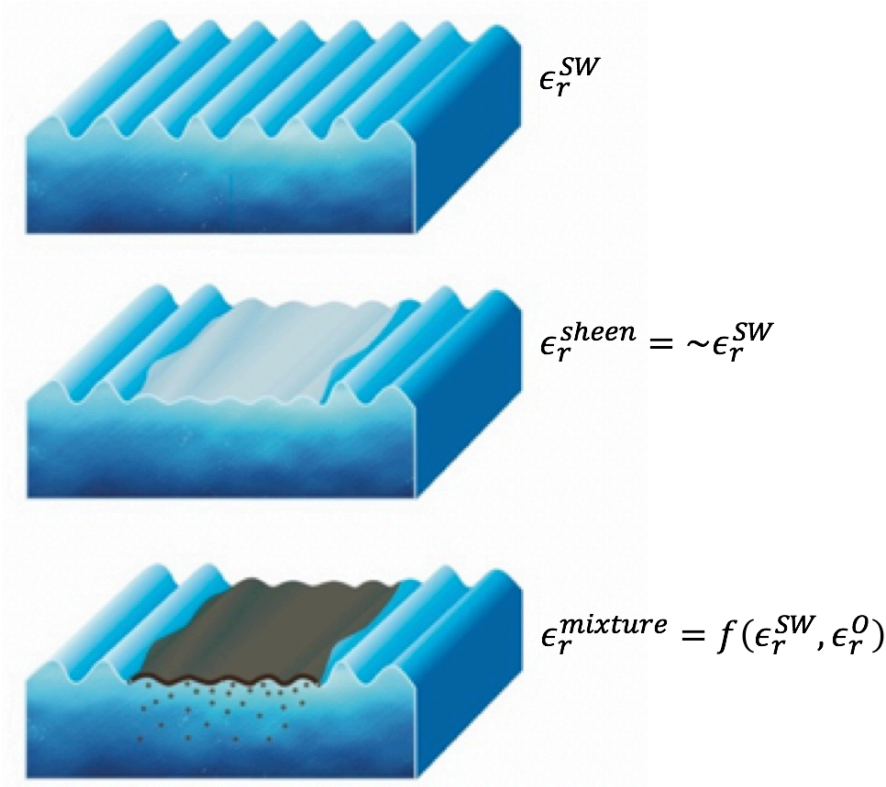

Figure 1.7 The impact of sheen and thicker mineral oil slicks on the relative dielectric constant. (Top) Clean sea water, (Middle) sheen slick, and (Bottom) thicker oil slick.

1.3.2 Surface scattering models

For the convenience of the reader, we proceed with a brief review of selected ocean surface scattering models adopted in the existing oil spill SAR literature, namely the small perturbation model (SPM), also referred to as the Bragg scattering model [43]; the two-scale model, also referred to as the composite model [43]; the Kudryavtsev model [44], which includes a depolarizing scattering mechanism; and the extended Bragg (X-Bragg) model, a polarimetric surface scattering model originally developed for soil surface retrieval [39], but also applied to marine oil spill studies [45]. Table 1.5 summarizes which surface properties are taken into account and which normalized radar cross-section (NRCS) components, σ_0, are represented in the ocean scattering models considered here.

Table 1.5 Overview of selected ocean surface scattering models. Co-polarization ratio: $PR \equiv \sigma_0^{HH}/\sigma_0^{VV}$.

Model	**Surface properties taken into account**	**NRCS components represented**	**PR function of**
SPM [43].	Ocean waves of wave-number $2k_r \sin\theta$ (Bragg wavenumber).	$\sigma_0^{pp} = \sigma_{0B}^{(1)pp}$, where $pp \in \{HH, VV\}$ and (1) indicates first order. Depolarization effects not included and $\sigma_{0B}^{(1)pq} = 0$, where $pq \in \{HV, VH\}$.	θ, ϵ_r
Two-scale model [43].	Adds tilt modulation by longer gravity waves to SPM.	$\sigma_0^{pp} = \sigma_{0B}^{pp}$ *and* $\sigma_0^{pq} = \sigma_{0B}^{pq}$ Cross-polarization term included.	$\theta, \epsilon_r, \psi, \xi$
Kudryavtsev model [44].	Adds depolarized scattering to 2-scale co-polarized NRCS, attributed to wave breaking from "steep" and "rough" patches.	$\sigma_0^{pp} = \sigma_{0B}^{pp} + \sigma_n$ Nonpolarized scattering (non-Bragg scattering) term σ_n added. [σ_{0B}^{pq} not included].	$\theta, \epsilon_r, \psi, \xi, \sigma_n$

The scattering of electromagnetic waves from the ocean surface is often modelled through approximate solutions with assumptions on the dimensions of the scattering elements [30,39]. The SPM assumes the variation of the surface roughness to be small compared to λ_r, $k_r\sigma_z \ll 0.3$ [39], and has a limited range of validity in terms of the ocean surface. The first-order NRCS components are given by

$$\sigma_{0B}^{(1)pp} = 4\pi {k_r}^4 cos^4(\theta)\left|g_{pp}^{(1)}(\theta, \epsilon_r)\right|^2 W(0, 2k_r \sin\theta),$$

where $W(\cdot)$ is the 2D wavenumber spectral density of the surface roughness and $g_{pp}^{(1)}(\theta, \epsilon_r)$ are the first-order scattering coefficients, which only depend on θ and ϵ_r [43]. For an explicit expression of $g_{pp}^{(1)}(\theta, \epsilon_r)$ see [43]. The SPM model is popular [38], but does not include nonzero cross-polarized backscatter or depolarization effects. Note that in a polarimetric radar system, cross-polarization is nonnull cross-polarized covariance matrix elements and depolarization is a nonunity normalized co-polarization correlation coefficient or polarimetric coherence coefficient [39,46].

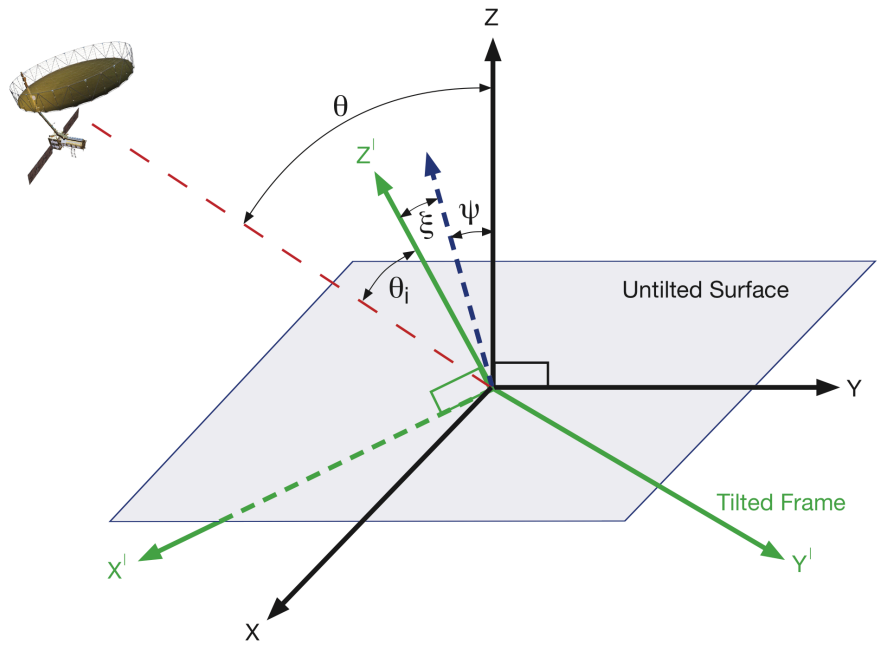

Figure 1.8 The SPM model assumes scatter from an untilted surface with incidence angle, θ, in the plane of incidence (the y-z plane as drawn). The two-scale model introduces tilted facets with in-plane tilt angle, ψ, and out-of-plane tilt angle, ξ, that characterize the rotation between the tilted surface normal, z', and the untilted surface normal, z.

Figure 1.8 illustrates the more realistic sea surface geometry introduced by the two-scale model, a modification of SPM that leads to a nonnull cross-polarization term [43]:

$$\sigma_{0B}^{pp} = 4\pi {k_r}^4 cos^4(\theta_i) \left| \left(\frac{\sin(\theta+\psi)\cos(\xi)}{\sin(\theta_i)} \right)^2 g_{pp}^{(1)}(\theta_i, \epsilon_r) + \left(\frac{\sin(\xi)}{\sin(\theta_i)} \right)^2 g_{qq}^{(1)}(\theta_i, \epsilon_r) \right|^2$$

$$\times W(2k_r \cos(\theta+\psi)\sin(\xi), 2k_r \sin(\theta+\psi))$$

and

$$\sigma_{0B}^{pq} = 4\pi {k_r}^2 cos^4(\theta_i) \left(\frac{\sin(\theta+\psi)\sin(\xi)\cos(\xi)}{sin^2(\theta_i)} \right)^2 \left| g_{VV}^{(1)}(\theta_i, \epsilon_r) - g_{HH}^{(1)}(\theta_i, \epsilon_r) \right|^2$$

$$\times W(2k_r \cos(\theta+\psi)\sin(\xi), 2k_r \sin(\theta+\psi)),$$

where $\sigma_{0B}^{HV} = \sigma_{0B}^{VH}$, θ is the local incidence angle relative to the untilted horizontal plane, and $\theta_i = cos^{-1}[\cos(\theta+\psi)\cos(\xi)]$ is the incidence angle for the tilted facet[3]. Now the first order scattering coefficients depend upon the facet geometry in

[3] See «Notes on further reading» at the end of the chapter for more information about this topic.

addition to the dielectric properties of the scattering surface [43]. Within the two-scale model, due to long gravity waves, the normal to the facet deviates from the vertical by an angle ψ in the plane of incidence and by an angle ξ in the plane perpendicular to the plane of incidence. Note that in this model $\sigma_{0B}^{pq} = 0$ if $\xi = 0$, i.e., if there is no out-of-plane tilt of the facet.

Building on the two-scale model, Kudryavtsev *et al.* [44] represented each co-polarized NRCS as the sum of one σ_{0B}^{pp} component associated with conventional two-scale Bragg scattering and one nonpolarized scattering component, σ_n, due to non-Bragg scattering. The non-Bragg component is assumed to be the same for VV and HH, and is interpreted as being caused by wave breaking from steep and rough patches on the sea surfaces and other phenomena that can cause non-Bragg scattering [44,30]. A cross-polarization term is not included in this model. The non-Bragg contribution can in theory be removed using the polarization difference PD:

$$PD \equiv \sigma_0^{VV} - \sigma_0^{HH} = \sigma_{0B}^{VV} - \sigma_{0B}^{HH}$$

The PD has been explored in oil spill studies and is reported to have good detection capability [47, and references therein].

Considering the robustness of the SMP model within its validity range [39], the X-Bragg model is a polarimetric model that attempts to widen the SPM model's validity range by allowing a random tilt of the facet, with the width of the distribution reflecting the roughness variability. It accounts for both cross-polarization and depolarization effects introduced through roughness-induced rotation of the Bragg coherency matrix (***T***-matrix, see, e.g., [10]) about an angle β in the plane perpendicular to the scattering plane. Assuming $P(\beta)$ to be a uniform distribution about zero with half-width β_1, the coherency matrix of the X-Bragg model is represented as [39]:

$$\boldsymbol{T} = \begin{bmatrix} T_{11} & T_{12} & T_{13} \\ T_{21} & T_{22} & T_{23} \\ T_{31} & T_{32} & T_{33} \end{bmatrix} = \begin{bmatrix} C_1 & C_2\,\mathrm{sinc}(2\beta_1) & 0 \\ C_2\,\mathrm{sinc}(2\beta_1) & C_3(1+\mathrm{sinc}(4\beta_1)) & 0 \\ 0 & 0 & C_3(1-\mathrm{sinc}(4\beta_1)) \end{bmatrix},$$

where $C_1 = \left|g_{HH}^{(1)} + g_{VV}^{(1)}\right|^2$, $C_2 = \left(g_{HH}^{(1)} + g_{VV}^{(1)}\right)\left(g_{HH}^{(1)*} - g_{VV}^{(1)*}\right)$, and $C_3 = 1/2\left|g_{HH}^{(1)} - g_{VV}^{(1)}\right|^2$. A couple of interesting features could be derived from the extended Bragg model:

$$R(\beta_1) = (T_{22} - T_{33})/(T_{22} + T_{33}) \text{ and } M(\theta, \epsilon_r) = (T_{22} + T_{33})/T_{11},$$

where *R* is a roughness indicator (depending only on the orientation angle), and *M* is a material indicator (depending on the incidence angle and the dielectric constant). These features have been explored in oil spill studies and varying sensitivity to different oil spill types has been reported [48,49]. Note that both of these features involve cross-polarization terms and, hence, caution should be used when applied to low signal-to-noise ratio (SNR) systems (see section 1.3.3).

According to Gade *et al.* [31], in the Marangoni damping theory, monomolecular slicks[4], such as natural biogenic slicks, show a resonance damping

[4] See «Notes on further reading» at the end of the chapter for more information about this topic.

behaviour that is absent for mineral oil slicks. Hence, the theory of Marangoni damping is left out of this discussion, as the primary focus here is on crude oil or emulsions with a thickness larger than monomolecular films and different damping mechanisms acting on the ocean surface waves.

1.3.2.1 Interpreting the co-polarization ratio from real SAR imagery

An appealing property of the SPM is that the roughness cancels in the co-polarization ratio and it only depends on the local incidence angle (relative to the untilted horizontal plane) and the dielectric properties of the media:

$$\frac{\sigma_0^{HH}}{\sigma_0^{VV}} = \frac{\left|g_{HH}^{(1)}(\theta,\epsilon_r)\right|^2}{\left|g_{VV}^{(1)}(\theta,\epsilon_r)\right|^2}$$

In the two-scale model, the co-polarization ratio depends on the large-scale roughness (through the tilt angles), the local incidence angle, and the dielectric properties of the media:

$$\frac{\sigma_0^{HH}}{\sigma_0^{VV}} = \frac{\left|\left(\frac{\sin(\theta+\psi)\cos(\xi)}{\sin(\theta_i)}\right)^2 g_{HH}^{(1)}(\theta_i,\epsilon_r) + \left(\frac{\sin(\xi)}{\sin(\theta_i)}\right)^2 g_{VV}^{(1)}(\theta_i,\epsilon_r)\right|^2}{\left|\left(\frac{\sin(\theta+\psi)\cos(\xi)}{\sin(\theta_i)}\right)^2 g_{VV}^{(1)}(\theta_i,\epsilon_r) + \left(\frac{\sin(\xi)}{\sin(\theta_i)}\right)^2 g_{HH}^{(1)}(\theta_i,\epsilon_r)\right|^2}$$

If the HH, VV, and HV NRCS values are known for the clean sea surface, the two ratios of the polarization dependent cross-section terms, $\sigma_0^{HH}/\sigma_0^{VV}$ and $\sigma_0^{HV}/\sigma_0^{VV}$, measured in the clean water can be used to solve for the two tilt angles. Under the assumption that the longer wavelengths on the sea surface are unaffected by the presence of a slick, the angles derived from the clean water can be used as an estimate for the slick covered surface [10]. Then, assuming the two-scale model is a good estimate for the surface scattering for both oil and water, the co-polarization ratio can be used to estimate ϵ_r for the oil slick.

In the Kudryavtsev model, the ocean wave spectral density term does not cancel in the co-polarization ratio,

$$\frac{\sigma_0^{HH}}{\sigma_0^{VV}} = \frac{\sigma_{0B}^{HH} + \sigma_n}{\sigma_{0B}^{VV} + \sigma_n},$$

so the ratio also depends on the nonpolarized scattering component. We note that the Kudryavtsev model explicitly assumes the added scattering mechanism is depolarizing in nature, mixing HH and VV. However, any added scattering component that is non-Bragg, e.g., incoherent surface scattering from other wave components, alters the co-polarization ratio from the SPM and two-scale models' situation in which ϵ_r can be calculated if only the imaging and surface geometry are known, i.e., no information about the wave spectra is required.

Figure 1.9 presents the co-polarization ratios corresponding to the three scenes shown in Figure 1.4. The Brage oil production slick, which is produced water (left panel), shows negligible contrast with that of clean water, so according to the SPM, the small fractions of oil contained in the produced water is too low to have an impact on the relative dielectric constant [Oil discharge measured to be 56 kg on day of

acquisition; Brage platform, personal communication 2018]. Considering the two-scale model, we can also ignore large-scale tilt variation between clean water and the slick. The middle and right panels show the co-polarization ratio for the two thicker oil emulsion slicks, which show a clear contrast to the surrounding sea. (Information about the releases in the right panel can be found in [50]). According to the theories described above, this is due to a change in the dielectric properties, damping of the large-scale roughness, or non-Bragg scattering. The small plant oil spill located to the upper left of the large emulsion slick in the right panel, exhibits a clear but weaker contrast to the surrounding sea water. Being a monomolecular slick no change in ε_r is expected. Therefore, the SPM theory does not hold because it predicts no contrast should be visible in the co-polarization ratio; which indeed is the case for the plant oil spill in the middle panel (compare with Figure 1.4). The two-scale model predicts the same as SPM for the plant oil slick if the large-scale roughness (facet tilt angles) are not modified between oil and clean sea. Instrument noise or non-Bragg scattering components could account for this. Note that the scene in the right-most panel was acquired with slightly higher incidence angles as compared to the other two scenes.

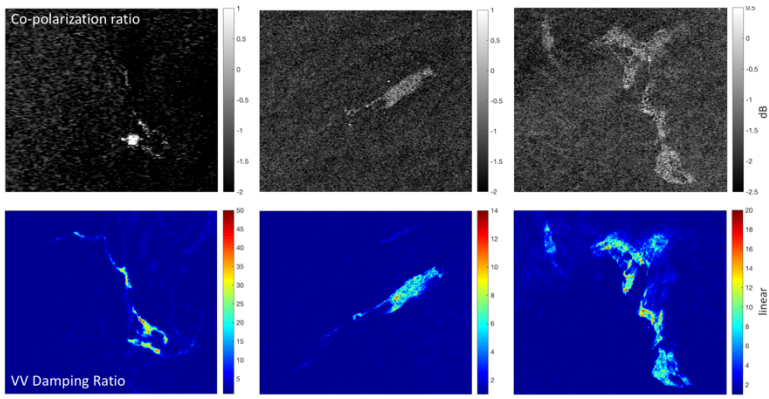

Figure 1.9 (Top) Co-polarization ratios in dB corresponding to the panels in Figure 1.4. (Bottom) VV-intensity damping ratio (contrast) in linear units. These are derived from Radarsat-2 C-band quad-polarization data.

Figure 1.10 shows the co-polarization ratio for two L-band QP scenes acquired with UAVSAR for which the NESZ is well below the slick intensities. In this case, the value for the slick in the North Sea (top), which has thickness 1.3-1.7 μm [51], agrees well with SPM and the two-scale model, but the value for the slick in the Gulf of Mexico shows good contrast with the clean water, even in areas where visual images show sheen. This, too, argues for another factor, either modification of the large-scale roughness and/or a non-Bragg scattering component. It is interesting to note that the North Sea image was acquired at winds of ~10 m/s and with visible wave breaking, but the Gulf image was acquired at wind speed 5 m/s and calm water. This argues for a non-Bragg scattering mechanism not driven solely by wave breaking.

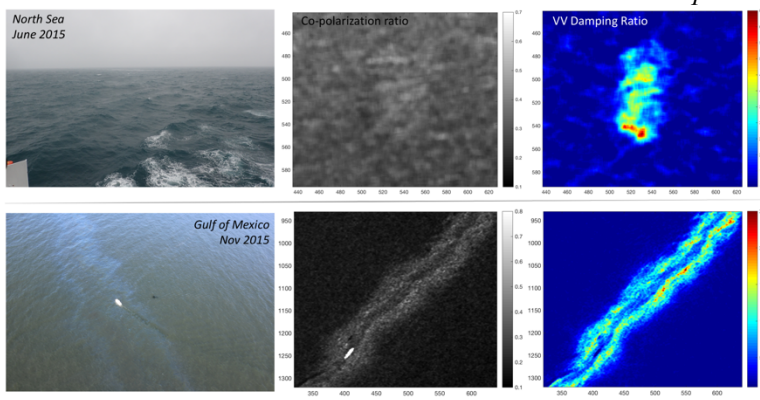

Figure 1.10 (Left) Photo of sea surface conditions, (Middle) co-polarization ratios in dB, and (Right) VV-intensity damping ratio (contrast) in linear units for acquisitions in the (top row) North Sea and (bottom row) Gulf of Mexico (GOM). The bright object in the GOM co-polarization ratio is the ship seen in the photo. Wind speed was 10 m/s (North Sea) and 5 m/s (GOM). In both cases, the oil slick is mainly sheen, but in one case the co-polarization ratio shows little contrast with clean water and in the other it shows 0.5 dB or larger contrast. Products are derived from UAVSAR L-band quad-polarization data.

1.3.2.2 Interpreting the damping ratio from real SAR imagery

In line with the SPM scattering theory discussed above, the damping ratio for an oil slick would be expressed as:

$$\frac{\sigma_{0,sea}^{VV}}{\sigma_{0,oil}^{VV}} = \frac{\left|g_{VV}^{(1)}(\theta,\epsilon_{r,sea})\right|^2}{\left|g_{VV}^{(1)}(\theta,\epsilon_{r,oil})\right|^2} \times \frac{W_{sea}(0,2k_r\sin\theta)}{W_{oil}(0,2k_r\sin\theta)}$$

Within the two-scale mode, the damping ratio would be expressed as:

$$\frac{\sigma_{0,sea}^{VV}}{\sigma_{0,oil}^{VV}} = \frac{\left|\left(\frac{\sin(\theta+\psi)\cos(\xi)}{\sin(\theta_i)}\right)^2 g_{VV}^{(1)}(\theta_i,\epsilon_{r,sea}) + \left(\frac{\sin(\xi)}{\sin(\theta_i)}\right)^2 g_{HH}^{(1)}(\theta_i,\epsilon_{r,sea})\right|^2}{\left|\left(\frac{\sin(\theta+\psi)\cos(\xi)}{\sin(\theta_i)}\right)^2 g_{VV}^{(1)}(\theta_i,\epsilon_{r,oil}) + \left(\frac{\sin(\xi)}{\sin(\theta_i)}\right)^2 g_{HH}^{(1)}(\theta_i,\epsilon_{r,oil})\right|^2} \times \frac{W_{sea}(2k_r\cos(\theta+\psi)\sin(\xi), 2k_r\sin(\theta+\psi))}{W_{oil}(2k_r\cos(\theta+\psi)\sin(\xi), 2k_r\sin(\theta+\psi))}$$

According to both scattering models, for either a monomolecular slick or a thin oil spill with a small thickness compared to the penetration depth of the radar [31], no change in ε_r is expected and the first factor of the damping ratio will hence be unity. Wave damping within the oil slick will be the only contrast driving factor. However, for a thicker slick, ε_r will change between sea and oil and hence both factors will contribute as contrast drivers between the oil slick and the surrounding sea water. Figure 1.9 and 1.10 show the damping ratios along with the co-polarization ratios for the five oil slick cases discussed above. In all cases, the damping ratio shows contrast within the slick, not just between the slick and clean water, indicative of zones of thicker or more emulsified oil.

1.3.3 Influence of instrument noise

The noise-equivalent sigma zero (NESZ), or *noise floor*, is a measure of the sensitivity of the SAR system to areas with low radar backscatter, and is given by a SNR, i.e., the ratio between backscatter level and the sensor NESZ, equal to 1 on a linear scale [52]. The NESZ is a function of slant range [52], and the backscattered signal's proximity to the noise floor has a significant influence on radar-dark measurements, which can lead to misinterpretation of SAR data. This is not an issue for spill detection (as long as the contrast between the oil slick and the surrounding clean sea is sufficient), where location and extent are determined, but the SNR should be considered carefully when slick characterization is the aim, so that the contribution from noise is not misinterpreted as a physical property of the scattering medium.

The influence of noise on derived quantities is illustrated using the damping ratio, which is known to increase with increasing Bragg wavenumber [31] and decrease with increasing wind speed [8]. Figure 1.11 shows how the damping ratio is influenced by SNR using data from oil spills measured with TerraSAR-X, Radarsat-2, and UAVSAR. The UAVSAR provides L-band ($\lambda_r = 23.8\,cm$) quad-polarimetric SAR measurements with a SNR that surpasses many spaceborne missions, including Radarsat-2 and TerraSAR-X [53]. The sensor covers a large range of incidence angles, $19.5° - 67.5°$, in a single scene [53], and the Bragg wavenumbers ranges from $17.6\,rad/m - 48.8\,rad/m$, depending upon incidence angle, with higher values in the far range. The measurements show that as the signal from the slick approaches the NESZ, the damping ratio increases, but at very low SNR the damping ratio again decreases. A threshold of 6 dB above the noise floor has previously been suggested as a guard margin for any scattering analysis, where estimated backscatter contributions within or below this range should be ignored [10].

Following [54], for a polarimetric SAR system, and assuming that the noise terms in the different polarization channels are uncorrelated with each other and with the signal, the measurement $\mathcal{M}$ should be related to the scattering matrix of interest as follows:

$$\mathcal{M} = \begin{bmatrix} M_{HH} & M_{VH} \\ M_{HV} & M_{VV} \end{bmatrix} = \begin{bmatrix} S_{HH} & S_{VH} \\ S_{HV} & S_{VV} \end{bmatrix} + \begin{bmatrix} n_{HH} & n_{VH} \\ n_{HV} & n_{VV} \end{bmatrix},$$

where n_{tr} represents the additive noise in channel tr characterized by a complex zero-mean Gaussian distribution. Many recent oil spill studies are investigating the potential of slick discrimination and characterization in polarimetric SAR systems (see, e.g., [4, 10]). A large range of multi-polarization SAR features have been explored in the literature [see, e.g., Table III in 55]. Gaining less attention is the fact that the impact of instrument noise will vary depending on how the selected feature is defined. Features involving more NRCS terms are more sensitive to noise contamination. To demonstrate, we denote the covariance matrix $C_{\mathcal{M}}$ for a linearly polarized system (d=3 when assuming reciprocity), obtained from the outer product of the scattering vector of the measurement:

$$C_{\mathcal{M}} = \begin{bmatrix} \langle M_{HH} \cdot M_{HH}^* \rangle & \sqrt{2}\langle M_{HH} \cdot M_{HV}^* \rangle & \langle M_{HH} \cdot M_{VV}^* \rangle \\ \sqrt{2}\langle M_{HV} \cdot M_{HH}^* \rangle & 2\langle |M_{HV}|^2 \rangle & \sqrt{2}\langle M_{HV} \cdot M_{VV}^* \rangle \\ \langle M_{VV} \cdot M_{HH}^* \rangle & \sqrt{2}\langle M_{VV} \cdot M_{HV}^* \rangle & \langle M_{VV} \cdot M_{VV}^* \rangle \end{bmatrix}$$

In a QP linearly polarized system, the H-polarization and V-polarization pulses are transmitted sequentially, not simultaneously. Because n_{HH} and n_{VV} are measured at different times, they are uncorrelated. A closer look at some of the matrix elements above shed light upon the influence of the noise term: For the co-polarization cross-product $\langle M_{HH} \cdot M_{VV}^* \rangle = \langle S_{HH} \cdot S_{VV}^* \rangle$ because the additive noise components decorrelate, but $\langle M_{VV} \cdot M_{VV}^* \rangle = |S_{VV}|^2 + \sigma_{VV}^n$, where σ_{VV}^n is the noise power (NESZ) [54].

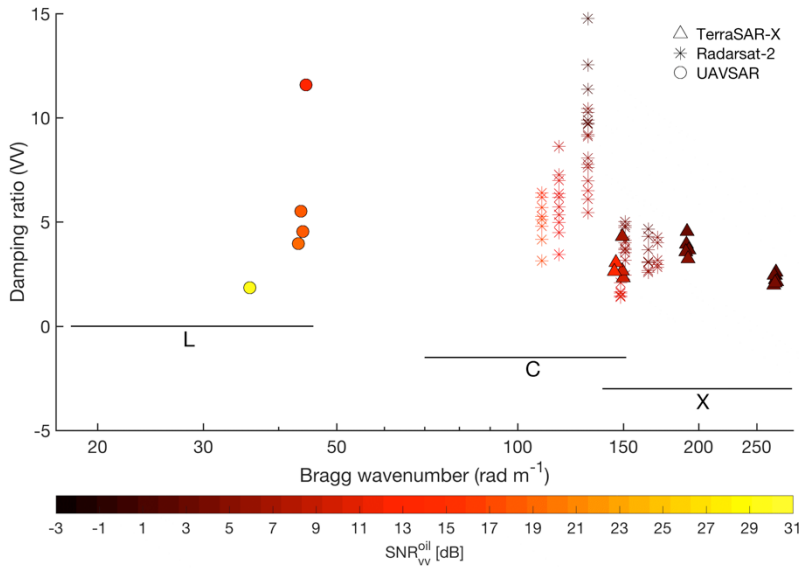

Figure 1.11 VV polarization clean sea/slick damping ratio on linear scale (y-axis, linear scale) versus Bragg wavenumber (x-axis). Markers are colour coded to indicate the SNR within mineral oil slicks. Each data point represents the mean of 728 pixels, irrespective of image resolution, which varies across the three SAR systems. The data samples are collected from multiple locations within slicks in scenes with different acquisition dates, metocean conditions, incidence angles and mineral oil properties. Figure is courtesy of Martine M. Espeseth.

1.4 Dark slick detection & characterization techniques

Early quad-polarimetric SAR missions such as the spaceborne imaging radar-C/X-band SAR (SIR-C/X-SAR) system, flown on the space shuttle Endeavor in 1994, paved the way for a new era in studies of sea surface slicks (see, e.g., [8]). However, the research field of oil spill observation by polarimetric SAR has had more rapid growth since the launch of TerraSAR-X in 2007, which first provided coherent dual-polarization (VV and HH) SAR imagery to the scientific community, and the launch of Radarsat-2 with its quad-polarimetic imaging capability later that year. This

section mainly covers techniques emerging within the last decade, and most of them are as yet in a pre-operational stage. We discuss both slick detection, i.e., a binary identification of oil spill vs. no oil spill on the sea surface, and slick characterization, i.e., quantitative or semi-quantitative measurement of a property of the material within the slick.

1.4.1 Slick detection and segmentation

Screening of traditional single-polarization SAR imagery for oil spill detection has commonly been framed into three fundamental steps: dark patch segmentation, feature extraction, and oil spill versus look-alike classification. Traditional methods rely on features extracted from the segmented patches (see, e.g, [56]). The features can be divided into the following categories: geometry and shape of the segmented patch, physical characteristics of the backscatter level of the segmented patch, contextual features, and texture [36]. The features are input into a classifier to separate potential oil spills from other types of look-alike dark patches. Commonly, the segmentation stage involves histogram thresholding or unsupervised segmentation procedures applied to the intensity levels of either the VV or HH polarization SAR channels only [56, 57]. More recently, application-generic segmentation approaches taking as input quad-polarimetric SAR data have emerged. Examples are methods involving modelling of the multi-looked sample complex covariance matrix [58] or multi-polarization SAR feature-based clustering [59]. Figure 1.12 shows a segmentation result of an oil spill derived from an unsupervised *K*-Wishart mixture model clustering approach incorporating Markov Random Field smoothing [58] to which the user inputs only the number of classes to be found. Before adopting this kind of method operationally, one should consider how sheen regions, which are often diffuse transitions from the oil spill to the ambient sea water, are handled by the various segmentation algorithms available. It is worth noting that any feature describing, e.g., the geometry of the segmented patch or the contrast between the average numerical feature values from the interior of the patch and the average numerical feature values from the nearby surrounding clean sea, will be sensitive to the level of constraint placed on the segment perimeter.

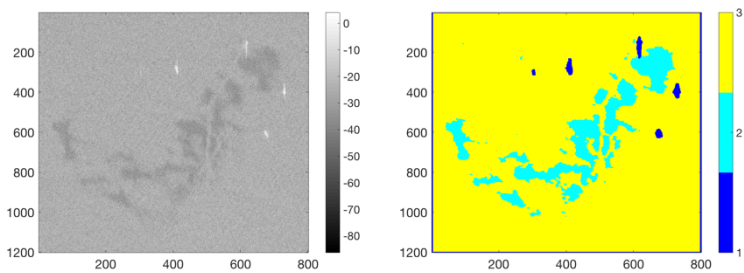

Figure 1.12 (Left) Emulsion oil slick shown in left panel of Figure 1.2. (Right) Segmentation example from a 3 class K-Wishart clustering algorithm. Based on auxiliary information, classes are 1) vessels, 2) oil spill, and 3) sea water. Segmentation algorithm is courtesy of Anthony P. Doulgeris. Figure produced by authors.

1.4.2 Slick type discrimination

In recent years, a large number of studies have been devoted to multipolarization SAR feature selection for sea surface slick detection or characterization. Table 1.6 gives an overview of a subset of the descriptors discussed in the literature. The features are often computed based on HH and VV polarization channels only, with the cross-polarization channels discarded due to additive noise contamination in low SNR measurements. We follow this approach to emphasize features that are applicable to both airborne (in general high SNR) and spaceborne (in general lower SNR) sensors. A categorization based on each feature's relation to the two-scale Bragg model equations (see section 1.3.2) has been proposed [55] and is adopted in Table 1.6. Category I contains features that depend on large- and small-scale roughness, incidence angle, and the relative dielectric constant, whereas the features in category II only depend on large-scale roughness, incidence angle, and the relative dielectric constant. These category II features are parameters for which the wave spectrum cancels in a ratio. Note that this categorization is based on the two-scale Bragg model, so the classification of features is not valid outside its validity range.

Table 1.6 Selected multi-polarization SAR features discussed in the oil spill literature. The categorization follows [55]. $\det(\cdot)$ *denotes the determinant,* $\boldsymbol{T}_2$ *denote the coherency matrix for the dual-polarization (VV and HH) case (see [4] eq. (6)),* $p_i = \lambda_i/(\lambda_1 + \lambda_2)$ *and* $\lambda_i(\lambda_1 > \lambda_2)$ *are the eigenvalues of* $\boldsymbol{T}_2$*, and* $\Re$ *denotes the real part. The superscript ' is used to distinguish the co-polarization version of a parameter from the conventional version. The list of references is not exhaustive.*

Category	#	Feature name	Definition	Reference
I	F1	Damping ratio	$DP = \frac{\langle \lvert S_{VV}\rvert^2\rangle_{sea}}{\langle \lvert S_{VV}\rvert^2\rangle_{oil}}$	[10,55,67]
	F2	Pol. difference	$PD = \langle \lvert S_{VV}\rvert^2\rangle - \langle \lvert S_{HH}\rvert^2\rangle$	[44,47,55]
	F3	Real part of co-pol. cross-product	$r_{co} = \lvert\Re(\langle S_{HH}\cdot S_{VV}^*\rangle)\rvert$	[4,47,55,61]
	F4	Span	$span' = \langle \lvert S_{HH}\rvert^2\rangle + \langle \lvert S_{VV}\rvert^2\rangle$	[63,47,55,65]
	F5	Largest eigenvalue	λ_1'	[10,47,55]
	F6	Geometric intensity	$\mu' = \left(det(\boldsymbol{T}_2)\right)^{1/2}$	[4,47,61]
II	F7	Co-pol. ratio	$PR = \frac{\langle \lvert S_{HH}\rvert^2\rangle}{\langle \lvert S_{VV}\rvert^2\rangle}$	[4,10,44,47,55]*
	F8	Entropy	$H' = -\sum_{i=1}^{2} p_i log_2 p_i$	[4,10,47,55,61, 62,63,64]
	F9	Anistropy	$A' = \frac{\lambda_1' - \lambda_2'}{\lambda_1' + \lambda_2'}$	[4,10,47,55, 61,62,63,64,65]
	F10	Std. dev. of co-pol. phase difference	$\sigma_{\phi co} = \sqrt{\langle(\phi_{HH} - \phi_{VV})^2\rangle - (\langle\phi_{HH} - \phi_{VV}\rangle)^2}$	[4,10,47,55,61,63, 64]

* In the literature, PR is either defined as VV/HH or HH/VV.

A feature selection analysis was done in [4], involving features from both category I and II. Out of eight multi-polarization SAR features that were investigated and extracted from Radarsat-2 quad-polarimetric measurements, the study concludes that the real part of the co-polarization cross product (F3) and the geometric intensity

(F6) are the most powerful features for biogenic vs. mineral oil spill discrimination. Both F3 and F6 belong to category I. In theory and from discussions in section 1.3, category I features should be more useful than category II features for capturing the difference in damping of surface roughness between biogenic and mineral oil slicks. Figure 1.13 shows the result from a clustering algorithm taking as input this particular feature vector $\{F3, F6\}$, and a clear separation between the upper left slick (plant oil) and the two lower slicks (emulsion and crude oil) is observed. For the mineral oil slicks, the boundary areas are assigned to the same class (green) as the monomolecular plant oil slick and are interpreted as thin sheen layers. In addition to this study, the potential of SAR for discriminating oil spills from low wind fields is reported in [44].

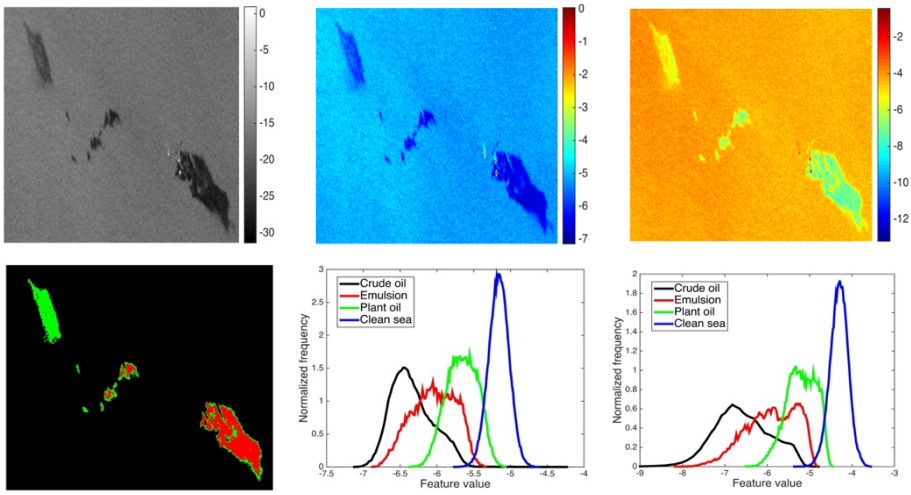

Figure 1.13 Top row, left to right: Intensity of SAR VV polarization channel [dB] containing oil slicks (plant oil (upper left), emulsion (middle) and crude oil (lower right)) from an oil-on-water exercise in 2011; F6; and F3. Bottom row, left to right: Classification of slick areas after ships and sea pixels are masked out; histogram of selected regions from the F6; and histogram of selected regions from F3. RADARSAT-2 Data and Products MDA LTD. (2011)—All Rights Reserved. Figure is courtesy of Stine Skrunes. Figure modified from [4].

More recent studies using high SNR airborne L-band SAR instruments have identified the most sensitive features for oil slick detection from QP data [55,68]. In both studies, the VV-intensity damping ratio (F1) and the polarization difference (F2) outperformed other investigated features, when considering those only using the co-polarized channel data. When including cross-polarization data also, both found the HV-intensity damping ratio to be a good discriminator, and [55], who considered more features, included the QP geometric intensity (F6) in the well-performing set. HP features was synthesized from QP UAVSAR data by [55], and the co-polarized and cross-polarized data's damping ratios were the highest performance features. It is interesting to note that most of the best features do not require polarimetric data, but use only the intensities. Oil thickness and concentration are key information needed to effectively target countermeasures during a major oil

spill incident. However, thickness has proven to be challenging to obtain by any remote sensor [69] and there are few operational methods available [1]. In infra-red (IR) remote sensing, an oil slick that is solar heated emits IR radiation as oil shows greater emissivity than water; thick oil appears "hot", intermediate thicknesses "cool", and thinner layers like sheen is not detectable [1]. In theory, the contrast drivers of oil spills in SAR measurements discussed in section 1.3.1 should be affected by thicker regions of oil. In Figure 1.14, airborne IR imagery from a surveillance aircraft is used to spatially identify the thicker regions within the oil slick imaged by space-borne SAR. The positions of the thick oil are estimated from the position of the aircraft and camera angles, and plotted as black markers (left panel). The damping ratio of the C-band SAR VV polarization channel exhibits the highest contrast between oil and water at locations where there is spatial overlap with thick oil observed by the IR camera, suggesting there is a potential in detecting thickness variations with SAR [60].

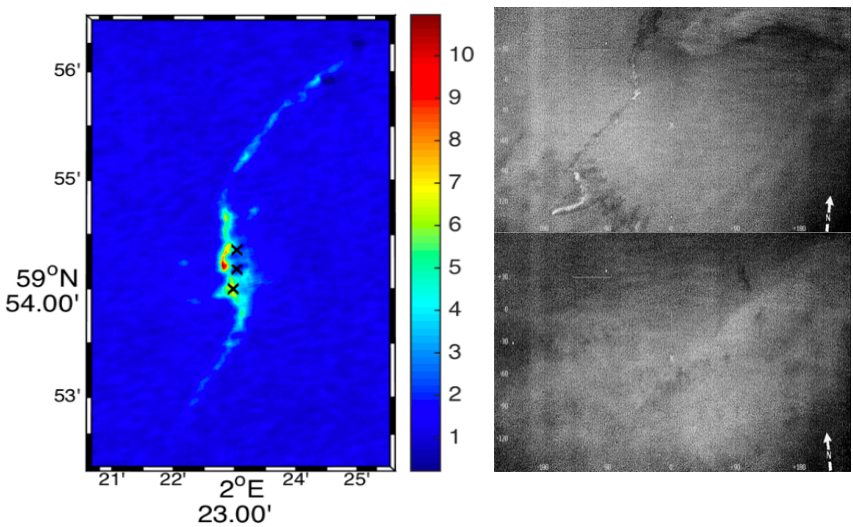

Figure 1.14 (Left) Damping ratio of a RISAT-1 FRS-2 scene (VV polarization channel) containing an oil slick in the North Sea. Positions of thicker oil estimated from aircraft data are indicated by 'x'. (Right) Aircraft data (infra-red images) provided by the Air Patrol Squadron Finland/SYKE. Figure is courtesy of Stine Skrunes. Figure adapted from [60].

At this point, relative, not quantitative, thickness determination has been accomplished [9,12,13]. Using data from a high SNR instrument, simple thresholds applied to the VV-damping ratio can be used to distinguish relative thickness. Figure 1.15 shows a slick separated into six relative thickness classes, with the evolution of transport and weathering shown in three images acquired at 1-hour intervals. Accumulation of oil along fronts is indicated for oil in the thickest two classes. In situ measurements taken in the area and overlapping with the first two acquisitions showed the area to be covered with sheen and patches of true color oil (thickness

from a few μm up to ~250 μm). Thickness classification using a neural network and based upon the entropy has also been done [12], but users of this parameter should be cognizant that the entropy is more sensitive to noise than the damping ratio [55].

Research efforts are currently directed towards developing methods for identifying zones of high oil concentration and estimating the volumetric fraction of oil from quad-polarimetric SAR imagery [10,11]. A method based upon the two-scale model and using the co-polarization ratio (see section 1.3.2.1) was pioneered in 2012 using data from the Deepwater Horizon [10]. The analysis indicated that the material in the slick had between 0.75 and 0.9 oil volumetric fraction. One issue with the method is that the model upon which it is based assumes that there is no contrast between the co-polarization ratio for sheen and clean water, which is not always the case (Figure 1.10). A recent refinement to the method using the Universal Weighted Curvature Approximation scattering model [66] obtained 0.49-0.52 oil volumetric fraction for a slick composed of emulsion of 40:60 oil-to-water ratio upon release in the North Sea [10]. While promising, the method needs validation and refinement to better agree with data for sheen slicks and to estimate the uncertainty in the derived oil volumetric fraction.

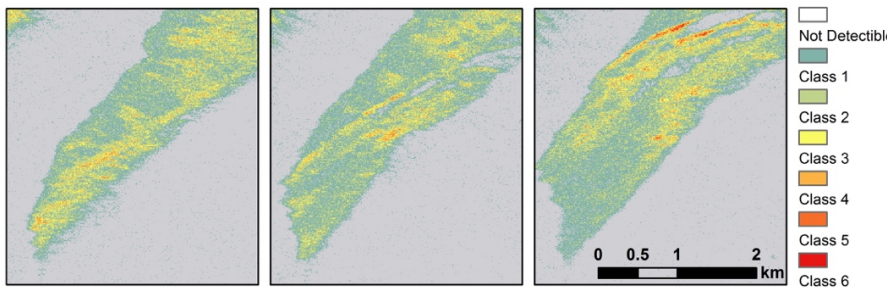

Figure 1.15 Relative thickness classification based upon thresholding the VV-intensity damping ratio of a slick from a seep in the MC20 block of the Gulf of Mexico. The series of images were separated in time by one hour each, with the earliest image on the left. In situ observations and measurements indicated that this area was mainly covered with sheen from silver to rainbow, with patches of discontinuous true color oil.

1.4.3 Slick transport and evolution

There are demands on both short and long timescales for information about the position of a slick from an oil spill (Table 1.1). In the short-term, the location and extent are most-immediately requested, while on longer timescales an estimate of the probable trajectory is wanted. With respect to nowcasts derived from SAR, a case study is reported in [70] in which a combination of a SAR image pair with 72 hours temporal baseline and auxiliary information on sea state and currents were used to determine possible oil spill drift. In general, with this temporal resolution, the spatial shape of the oil spill can be expected to have changed beyond recognition. As pointed out in section 1.1, drift estimations derived from spatial feature correlation requires two or more consecutive SAR images close in time (minutes to few hours). At this timescale, the derived velocity vector can be used as a nowcast product.

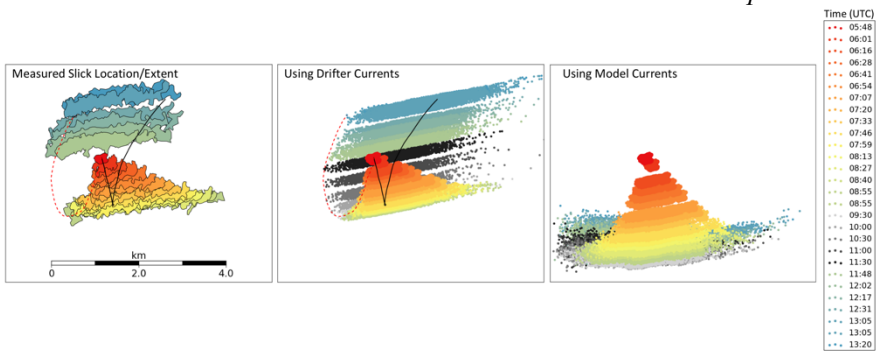

Figure 1.16 Comparison of the OpenOil drift model [https://github.com/knutfrode/opendrift] to measured slick transport using a rapid repeat time series of SAR images. An 0.5 m³ release of 80:20 oil:water emulsion was measured (left) and modeled (middle, right). Results from modelling based on currents from co-released drifters (middle) are more accurate than that using currents obtained from an ocean model (right). Figure modified from [74].

In remote areas and harsh environmental conditions, e.g., at high latitudes in the Arctic, the response will be slower compared to that at more temperate latitudes, and longer and more accurate forecasts are requested [71]. Numerous oil spill models have been developed over the years to provide forecasts, and it is beyond the scope of this chapter to give a comprehensive review. Three types of methods have been proposed for simulation of oil spill transport in water, all partitioning the oil volume into discrete pieces to be modelled numerically: (1) particle-tracking, (2) tracers, and (3) spillets [71][5]. An example of a pollutant particle ('splot') tracking model is the General NOAA Operational Modeling Environment (GNOME), which is initialized and compared to SAR imagery in [72,73]. In brief, to better understand marine oil spill transport, numerical models are used to simulate both vertical and horizontal transport mechanisms. Recent efforts to integrate numerical models with time-series of SAR measurements have led to several advancements within the field. First, a deeper understanding of the vertical exchange between the submerged oil droplets and the surface slick and how it impacts the slick signature in the SAR imagery has been gained. Second, improved models and prediction capabilities of the oil spill's horizontal transport have been developed [74,75]. Jones *et al*. [74] found that the agreement between theory and measurement (Figure 1.16) is improved significantly by local current measurements and that modeled wind fields are sufficient. The measurements shown were made at wind speeds from 9-12 m/s and used to calibrate the OpenOil [https://github.com/knutfrode/opendrift] model's droplet radii and entrainment length.

1.5 Concluding remarks and outlook

In this chapter, we have briefly explained the physical mechanisms behind radar

[5] See «Notes on further reading» at the end of the chapter for more information about this topic.

imaging of oil slicks at sea, discussed how scattering models can aid interpretation of SAR imagery, and visited emerging information retrieval techniques for providing some of the information items requested by the community. We discussed the available instruments and the limitations on their use for oil spill observations. C-band SAR has traditionally been used for ocean monitoring from space, e.g., ERS-1/-2, ENVISAT, Radarsat-1/-2, Sentinel-1, but there is increasing utilization of L-band and X-band missions, e.g., ALOS-PALSAR, ALOS-2, and TerraSAR-X, soon to be augmented by RCM, SAOCOM-1/2, and NISAR. The most important space-borne missions for operational environmental monitoring of the oceans are currently Radarsat-2, Sentinel-1, and the upcoming RCM, based on coverage, access to the data, operational modes and noise characteristics.

In section 1.1, we gave an overview of key information items involving SAR remote sensing. Those items can be split between those requiring *detection* of the spill and those requiring *characterization* of the released material. Information based on slick detection, such as position, extent, and drift forecasting, can be derived utilizing data from any of space-borne SAR missions and do not in general require a particular polarization mode, although the VV mode is preferable because of the higher backscatter levels. Efforts are now being made towards integration of remote sensing information with numerical oil transport models for hind-, now-, and fore-casting, and rapid repeat SAR time series images from airborne SAR have contributed to constraining model parameters [74,75]. The aim is to better predict the transport of the oil to serve coastal monitoring agencies. This work is found valuable and important to continue.

Oil characterization with SAR is not as far advanced insofar as operationalizing the methods, and much of the recent advancement has been made with airborne SAR specifically because the signals proximity to the noise floor is an issue for space-borne SAR sensors. For oil slick characterization purposes in particular, attention has to be payed to this problem. Three important usages of SAR-based characterization were discussed: look-alike discrimination, thickness measurement, and identification/measurement of emulsified oil. An important advancement in utilization of SAR for oil spill response will be in characterizing oil within the slick into categories that match recoverable or non-recoverable oil. At this point, relative thickness, potentially calibrated with in situ or ancillary data, has been demonstrated but not operationalized. Interestingly, contrast features (damping ratio) and the polarization difference are the features most sensitive to variations within slicks, and these require only intensity measurements. Quantifying emulsification via measurement of the oil volumetric fraction (oil:water ratio) requires multi-polarization data to extract information about the dielectric properties of the scattering medium. If we restrict the choice of transmit and receive electromagnetic wave polarization to only linear polarization, i.e., combinations of horizontal and vertical, information about the electrical characteristics of the slicks can only be obtained if both VV and HH products are available for the scene. A quad-polarimetric SAR system meets this requirement by alternating between transmitting H and V polarized pulses while receiving both. However, this requires twice the pulse-repetition frequency of a single- or dual-polarized system [76], which could cause interference between the received echoes. The upcoming NISAR mission can avoid this problem using for ocean imaging a quasi-quad-polarimetric split-spectrum mode in which V- and H-polarization pulses are transmitted simultaneously at

slightly different frequencies. The frequency diversity applied in the quasi-quad-polarimetric mode of NISAR and the multi-frequency opportunities from the range of space-borne platforms suggest more spectral investigative and frequency comparison studies in the future.

Progress has clearly been made in the field of oil spill characterization over the last decade or so, but there is still a need for more validation campaigns collecting in situ and auxiliary data, e.g., optical remote sensing measurements that could be used to assess the validity range and sensitivity of the algorithms and methods developed. This plus more advanced models with validation across a range of metocean conditions are key advancements needed for operationalization of SAR-based oil spill characterization. Airborne SAR, with its high SNR and rapid repeat capability could play an important role in response to major spills in the future. However, space-borne SAR will continue to be the main instrument for operational surveillance, particularly as more SAR missions are launched.

Notes on further reading

The two-scale model: See [45] for notes on a small refinement of the model.

Monomolecular slicks: Natural slicks of biogenic origin are common in coastal waters and open ocean, produced by, e.g., algae and bacteria. Unlike mineral oil slicks, biogenic surface films consist of surface-active organic compounds that have both a hydrophobic and a hydrophilic component. This combination causes the molecules to spontaneously arrange in a monomolecular layer at the air/water interface, with the hydrophobic part at the air interface and the hydrophilic part at the water interface. This forms a film one molecule thick (~ 2.4 to 2.7 nm) [77,78]. Crude oil spills consist mainly of alkanes, cycloalkanes, and aromatic compounds, chemicals that are exclusively hydrophobic. Without the combination of hydrophilic and hydrophobic parts, crude oil slicks do not form monomolecular films. Over time crude oil spills spread out into layers of different thickness depending on the amount and viscosity of the oil and on the environmental conditions, with the final thickness on the scale of micrometres to millimetres, and even centimetres for freshly spilled oil [77,78], much thicker than the monomolecular biogenic films.

Numerical drift modelling: In the *particle-tracking* approach, the distribution of particles represents the whole oil spill in a statistical fashion. The oil is parameterized as a finite number of particles that are assigned an initial location and mass and tracked numerically by a trajectory model. For the *tracers*, the tracking area of the oil spill is represented by a fine-resolution grid and the spill occupies the cells that represent its physical extent. The *spillet* method is close to the particle method but adds more degrees of freedom, such as the area or thickness represented by each spillet. This method can be seen as a compromise between the particle and tracer methods. More information about the advantages and drawbacks of the different methods can be found in [71].

Acknowledgement

This work is partly is financed by CIRFA (RCN Grant no. 237906). The work was carried out in part at the Jet Propulsion Laboratory, California Institute of Technology, under contract with the National Aeronautics and Space Administration. The authors thanks Martine Espeseth and Dr. Stine Skrunes for producing some of the figures for this chapter.

References

1 Fingas, M., Brown, C. E. 'A Review of Oil Spill Remote Sensing'. *Sensors*. 2018;**18**(1):1-18

2 Carpenter, A. 'European Maritime Safety Agency *CleanSeaNet* Activities in the North Sea' in Carpenter, A. (ed.). *Oil Pollution in the North Sea*. Switzerland: Springer; 2016. pp. 33-47

3 NOAA NESDIS – U.S. National Oceanic and Atmospheric Administration Satellite and Information Service. *NESDIS Marine Pollution Products* [online]. Available from https://www.ospo.noaa.gov/Products/ocean/marinepollution [Accessed 15 October 2018]

4 Skrunes, S., Brekke, C., Eltoft, T. 'Characterization of Marine Surface Slicks by Radarsat-2 Multipolarization Features'. *IEEE Transactions of Geoscience and Remote Sensing*. 2014; **52**(9):5302-5319

5 NOAA – National Oceanic and Atmospheric Administration U. S. Department of Commerce. *Characteristics of Response Strategies: A Guide for Spill Response Planning in Marine Environments* [online]. Available from https://response.restoration.noaa.gov/sites/default/files/Characteristics_Response_Strategies.pdf [Accessed 29 August 2018]

6 Bonn Agreement. *Bonn Agreement Oil Appearance Code, Bonn Agreement Aerial Operations Handbook, Part 3, Annex A, The Bonn Agreement Oil Appearance Code* [Online]. Available from https://www.bonnagreement.org/site/assets/files/1081/special_on_volume_calculation_20160607.docx [Accessed 13 August 2018]

7 NOAA Office of Response and Restoration. *Open Water Oil Identification Job Aid for aerial observation*, Version 3, August 2016 [Online]. Available from https://response.restoration.noaa.gov/sites/default/files/OWJA_2016.pdf [Accessed 29 October 2018]

8 Gade, M., Alpers, W. 'Imaging of biogenic and anthropogenic ocean surface films by the multifrequency/multipolarization SIR-C/X-SAR'. *Journal of Geophysical Research*. 1998;**103**(C9):18851-18866

9 Jones, C. E., Holt. B. 'Experimental L-band airborne SAR for oil spill response at sea and in coastal waters'. *Sensors*. 2018;**18**(2):13 pages

10 Minchew, B., Jones, C. E., Holt, B. 'Polarimetric analysis of backscatter from the Deepwater Horizon oil spill using L-Band synthetic aperture radar'. *IEEE Transactions on Geoscience and Remote Sensing*. 2012;**50**(10):3812-3830

11 Angelliaume, S., Boisot, O., Guérin, C.-A. 'Dual-Polarized L-Band SAR Imagery for Temporal Monitoring of Marine Oil Slick Concentration'. *Remote Sensing*. 2018;**10**(7):17 pages

12 Garcia-Pineda, O., MacDonald, I., Hu, C., Svejkovsky, J., Hess, M., Dukhovskoy, D., Morey, S.L. 'Detection of floating oil anomalies from the Deepwater Horizon oil spill with synthetic aperture radar.' *Oceanography*. 2013;**26**:124–137

13 Minchew, B. 'Determining the mixing of oil and sea water using polarimetric synthetic aperture radar'. *Geophysical Research Letters*. 2012;**39**:6 pages

14 Yu, F., Li, J., Cui, S., Zhao, Y., Feng, Q., Chen G. 'A hindcast method to simulate oil spill trajectories for Bohai Sea, Norteast China'. *Ocean Engineering*. 2016;**124**:363-370
15 Ly J. M., Alsos G. A., Brekke C., Enge S., Flogeland E., Kvamme L. J., *et al*. *Norsk oljevernberedskap – rustet for framtiden?* Technical report, Norwegian Ministry of Transportation and Communication, 2015
16 Raney, R.K. 'Hybrid-Polarity SAR Architecture'. *IEEE Transactions on Geoscience Remote Sensing*. 2007;**45**(11):3397–3404
17 MDA MacDonald, Dettwiler and Associates Ltd (Canada). *Radarsat-2 product description*. RN-SP-52-1238. Issue 1/13: March 21, 2016
18 Espeseth, M., Brekke, C., Johansson, M. A. 'Assessment of RISAT-1 and Radarsat-2 for Sea Ice Observations from a Hybrid-Polarity Perspective'. *Remote Sensing*. 2017;**9**(11):1-20
19 Holt, B. 'SAR imaging of the ocean surface' in Jackson C. and Apel J. (ed.). *Synthetic Aperture Radar Marine User's Manual*. U.S. Department of Commerce, National Oceanic and Atmospheric Administration, Washington DC, USA; 2004. pp. 25–80
20 Fritz, T., Eineder, M. (ed.). *TerraSAR-X Ground Segment, Basic Product Specification Document*. DLR, TX-GS-DD-3302, Issue 1.5, 2008
21 Italian Space Agency. *COSMO-SkyMed Mission and Products Description*. ASI, ASI-CSM-PMG-NT-001, Issue 2, 2016
22 Milillo, P., Fielding, E. J., Schulz, W. H., Delbridge, B. Bürgmann, R. 'COSMO-SkyMed spotlight interferometry over rural areas: The Slumgullion Landslide in Colorado, USA'. *IEEE Journal of Selected Topics in Applied Earth Observations and Remote Sensing*. 2014;**7**(7):2919-2926
23 Misra T., Rana, S.S., Desai, N. M., Dave, D. B., Rajeevjyoti, Arora, R. K., *et al*. 'Synthetic Aperture Radar payload on-board RISAT-1: configuration, technology and performance'. *Current Science*. 2013;**104**(4):446-461
24 Dabboor, M., Iris, S., Singhroy, V. 'The RADARSAT Constellation Mission in Support of Environmental Applications'. *Proceedings*. 2018;**2**(7):5 pages
25 Ren, L., Yang, J., Mouche, A., Wang, H., Wang, J., Zheng, G., Zhang, H. 'Preliminary analysis of Chinese GF-3 SAR quad-polarization measurements to extract wind in each polarization'. *Remote Sensing*. 2017;**9**(1215):1-17
26 JAXA – Japan Aerospace Exploration Agency. *ALOS-2/PALSAR-2 Calibration and Validation Results Ver. 2018.08.07* [online]. Available from https://www.eorc.jaxa.jp/ALOS-2/en/calval/PALSAR2_CalVal_Results_JAXA_201808.pdf [Accessed 8 November 2018]
27 Euillades, P. A., Euillades, L. D., Azcueta, M., Sosa, G. 'SAOCOM 1A Interferometric Error Model and Analysis'. *Proceedings of the Fringe 2015 Workshop*; Frascati, Italy, March 2015. Noordwijk: ESA Communications; 2015. 5 pages
28 Ren, Y., Li, X.-M., Zhou, G., 'Sea Surface Wind Retrievals from SIR-C/X-SAR Data: A Revisit'. *Remote Sensing*. 2015;**7**:3548-3564

29 Donelan, M. A., Pierson, W. J. 'Radar Scattering and Equilibrium Ranges in Wind-Generated Waves With Application to Scatterometry'. *Journal of Geophysical Research. 1987;**92**(C5):4971-5029*

30 Skrunes, S. *Characterization of Low Backscatter Regions in the Marine Environment by Multipolarization C- and X-band Synthetic Aperture Radar Data*. PhD thesis, UiT The Arctic University of Norway, 2014

31 Gade, M., Alpers, W., Hühnerfuss, H., Wismann, V. R., Lange, P. A. 'On the reduction of the radar backscatter by oceanic surface films: Scatterometer measurements and their theoretical interpretation'. *Remote Sensing of Environment*. 1998;**66**(1):52-70

32 Transportation Research Board and National Research Council. *Oil in the Sea III: Inputs, Fates, and Effects*. Washington, DC: The National Academies Press; 2003

33 Reed M., Johansen Ø., Brandvik P. J., Daling P., Lewis A., Fiocco R., *et al*. 'Oil Spill Modeling towards the Close of the 20th Century: Overview of the State of the Art'. *Spill Science & Technology Bulletin*. 1999;**5**(1):3-16

34 Hollinger, J. P, Mennella, R., A. 'Oil Spills: Measurements of Their Distributions and Volumes by Multifrequency Microwave Radiometry'. *Science,* New Series. 1973;**181**(4094):54-56

35 Visser, A.W. 'Using random walk models to simulate the vertical distribution of particles in a turbulent water column'. *Marine Ecology Progress Series*. 1997;**158**:275–281

36 Brekke, C., Solberg, A. H. S. 'Oil spill detection by satellite remote sensing'. *Remote Sensing of Environment*. 2005;**95**(1):1-13

37 Ulaby, F., Moore, R. K., Fung, A. K. *Microwave remote sensing, active and passive, volume II; Radar Remote Sensing and Emission Theory*. Norwood, USA: Artech House Inc.; 1986

38 Grahn, J., *Multi-frequency radar remote sensing of sea ice*. PhD thesis, UiT The Arctic Univeristy of Norway, 2018

39 Hajnsek, I., Pottier, E., Cloude, S. R. 'Inversion of surface parameters from polarimetric SAR'. *IEEE Transactions on Geoscience and Remote Sensing*. 2003;**41**(4):727-744

40 Elachi, C., Brown, W. E. 'Models of Radar Imaging of the Ocean Surface waves'. *IEEE Transactions on Antennas and Propagation*. 1977;**AP-25**(1):84-95

41 Hasselmann, K., Hasselmann, S. 'On the nonlinear mapping of an ocean wave spectrum into a synthetic aperture radar image spectrum and its inversion'. *JGR-Oceans*, 1991;**96**(C6):10713-10729

42 Jones, C. E., Minchew, B., Holt, B., Hensley, S. 'Studies of the Deepwater Horizon oil spill with the UAVSAR radar' in Liu, Y. *et al*. (Eds). *Monitoring and Modeling the Deepwater Horizon Oil Spill: A Record-Breaking Enterprise*. Washington D. C.: American Geophysical Union; 2011. pp. 33-50.

43 Valenzuela, G. R. 'Theories for the interaction of electromagnetic and oceanic waves – A review'. *Boundary-Layer Meteorology*. 1978;**13**(1-4):61-85

44 Kudryavtsev, V. N., Chapron, B., Myasoedev, A. G., Collard, F., Johannessen, J. 'On Dual Co-Polarized SAR Measurements of the Ocean Surface'. *IEEE Geoscience and Remote Sensing Letters*. 2013;**10**(4):761-765

45 Salberg, A.-B., Rudjord, Ø., Solberg, A. H. S. 'Oil Spill Detection in Hybrid-Polarimetric SAR Images'. *IEEE Transactions on Geoscience and Remote Sensing*. 2014;**52**(10):6521-6533
46 Iodice, A., Natale, A., Riccio, D. 'Retrieval of Soil Surface Parameters via a Polarimetric Two-Scale Model'. *IEEE Transactions on Geoscience and Remote Sensing*. 2011;**49**(7):2531-2547
47 Skrunes, S., Brekke, C., Jones, E. C., Espeseth, M. M., Holt, B. 'Effect on wind direction and incidence angle on polarimetric SAR observations of slicked and unslicked sea surfaces'. *Remote Sensing of Environment*. 2018;**213**:73-91
48 Rudjord, Ø., Salberg, A.-B. 'X-Bragg based detection of oil spills using polarimetric SAR'. *Proceedings of SeaSAR2012*; Tromsø, Norway, June 2012. Noordwijk: ESA Communications; 2013. 4 pages
49 Yin, J., Yang, J., Zhou, Z.-S., Song, J. 'The Extended Bragg Scattering Model-Based Method for Ship and Oil-Spill Observation Using Compact Polarimetric SAR'. *IEEE Journal of Selected Topics in Applied Earth Observation and Remote Sensing*. 2015;**8**(8):3760-3772
50 Skrunes, S., Brekke, C., Doulgeris, A. P. 'Characterization of Low-Backscatter Ocean Features in Dual-Copolarization SAR Using Log-Cumulants'. *IEEE Geoscience and Remote Sensing Letters*. 2015;**12**(4):836-840
51 Skrunes, S., C. Brekke, C. Jones, B. Holt. 'A Multisensor Comparison of Experimental Oil Spills in Polarimetric SAR for High Wind Conditions'. *Journal of Selected Topics in Applied Earth Observation and Remote Sensing*. 2016;**9**(1):4948-4961
52 Younis, M., Huber, S., Patyuchenko, A., Bordoni, F., Krieger, G. 'Performance Comparison of Reflector – and Planar-Antenna Based Digital Beam-Forming SAR'. *International Journal of Antennas and Propagation*, 2009;**2009**:13 pages
53 Skrunes, S., Brekke, C., Jones, C. E., Holt, B. 'A multisensor comparison of experimental oil spills in polarimetric SAR for high wind conditions'. *IEEE Journal of Selected Topics in Applied Earth Observations and Remote Sensing*. 2016; **9**(11):4948-4961
54 Freeman, A. 'The effects of noise on polarimetric SAR data'. *Proceedings of IGARSS'93 - IEEE International Geoscience and Remote Sensing Symposium*; Tokyo, Japan, August 1993. pp.799-802
55 Espeseth, M. M., Skrunes, S., Jones, C. E., Brekke, C., Holt, B., Doulgeris, A. P. 'Analysis of evolving oil spills in full-polarimetric and hybrid-polarity SAR'. *IEEE Transactions on Geoscience and Remote Sensing*. 2017;**55**(7):4190-4210
56 Solberg, A. S., Storvik, G., Solberg, R., Volden E. 'Automatic Detection of Oil Spills in ERS SAR Images'. *IEEE Transactions on Geoscience and Remote Sensing*. 1999;**37**(4):1916-1924
57 Derrode, S., Mercier, G. 'Unsupervised multiscale oil slick segmentation from SAR images using a vector HMC mode'. *Pattern Recognition*. 2007;**40**:1135-1147
58 Doulgeris, A. P., Anfinsen, S. N., Eltoft, T. 'Classification With a Non-Gaussian Model for PolSAR Data'. *IEEE Transactions on Geoscience and Remote Sensing*. 2008;**46**(10):2999-3009

59 Doulgeris, A. P. 'A simple and extendable segmentation method for mulit-polarization SAR images'. *Proceedings of POLinSAR*; Frascati, Rome, Italy, 2013. 8 pages

60 Skrunes, S., Brekke, C., Espeseth, M. M. 'Assessment of the RISAT-1 FRS-2 mode for oil spill observation'. Proceedings of *IGARSS 2017 - IEEE International Geoscience and Remote Sensing Symposium;* Forth Worth Texas, USA, July 2017. pp. 1024-1027

61 Migliaccio, M., Nunziata, F., Buono, A. 'SAR polarimetry for sea oil slick observation'. *International Journal of Remote Sensing*. 2015;**36**(12):3243-3273

62 Schuler, D. L., Lee, J.-S. 'Mapping ocean surface features using biogenic slick-fields and SAR polarimetric decomposition techniques'. *IEE Proceedings - Radar, Sonar and Navigation*. 2006;**153**(3):260-270

63 Wenguang, W., Fei, L., Peng, W., Jun, W. 'Oil Spill Detection from Polarimetric SAR Image'. *Proceedings of IEEE 10th International Conference on Signal Processing*; Beijing, China, October 2010. pp.832-835

64 Solberg, A. 'Remote Sensing of Ocean Oil-Spill Pollution'. *Proceedings of the IEEE*. 2012;**100**(10):2931-2945

65 Fortuny-Gausch, J. 'Improved oil slick detection and classification with polarimetric SAR'. *Proceedings of POLinSAR Workshop on Applications of SAR Polarimetry and Polarimetric Interferometry*; Frascati, Italy, January 2003. 5 pages

66 Guerin, C.-A., Soriano, G., Chapron, B. 'The weighted curvature approximation in scattering from sea surfaces'. *Waves Random Complex Media*. 2010;**20**:364–384.

67 Jones, C. E., Espeseth, M. M., Holt, B., Brekke, C., Skrunes, S. 'Characterization and discrimination of evolving mineral and plant oil slicks based on L-band synthetic aperture radar (SAR)'. *Proceedings of SPIE*, Edinburg, Uk 2016. 13 pages

68 Angelliaume, S., Dubois-Fernandez, P., Jones, C. E., Holt, B., Minchew, B., Amri, E., Miegebielle, V. 'SAR imagery for detecting sea surface slicks: Performance assessment of polarization-dependent parameters'. *IEEE Transactions on Geoscience and Remote Sensing*. 2018;**56**(8):4237-4257

69 Leifer, I., Lehr, W. J., Simecek-Beatty, D., Bradley, E., Clark, R., Dennison, P., *et al*. State of the art satellite and airborne marine oil spill remote sensing: Application to the BP Deepwater Horizon oil spill. *Remote Sensing of Environment*. 2012;**124**:185-209.

70 Fan, K., Zhang, Y., Lin, H. 'Satellite SAR analysis and interpretation of oil spill in the offshore water of Hong Kong'. *Annals of GIS*. 2010;**16**(4):269-275

71 Drozodowski, A., Nudds, S., Hannah, C. G., Niu, H. Peterson, I. K., Perrie, W. A. *Review of Oil Spill Trajectory Modelling in the Presence of Ice*. Canadian Technical Report of Hydrography and Ocean Sciences 274, Fisheries and Oceans Canada, 2011.

72 Xu, Q., Li, X., Wei, Y., Tang, Z., Cheng, Y., Pichel, W. G.'Satellite observations and modeling of oil spill trajectories in the Bohai Sea'. *Marine Pollution Bulletin. 2013;**71**:107-116*

73 Cheng, Y., Liu, B., Li, X., Nunziata, F., Xu, Q., Ding, X., *et al*. 'Monitoring of Oil Spill Trajectories With COSMO-SkyMed X-Band SAR Images and Model Simulation'. *IEEE Journal of Selected Topics in Applied Earth Observation and Remote Sensing*. 2014;**7**(7):2895-2901

74 Jones C. E., Dagestad K.-F., Breivik Ø., Holt B., Röhrs J., Christensen K. H., *et al*. 'Measurement and modelling of oil slick transport'. *Journal of Geophysical Research: Oceans*. 2016; **121**(10):7759-7775

75 Röhrs J., Dagestad K.-F., Asbjørnsen H., Nordam T., Skancke J., Jones C. E., *et al*. 'The effect of vertical mixing on the horizontal drift of oil spills'. *Ocean Science*. 2018 (in review)

76 Raney, R. K. 'A perspective on compact polarimetry'. *IEEE Geoscience and Remote Sensing Newsletter*. 2011;160:12-18

77 Alpers, W., Espedal, H. A. 'Oils and surfactants' in Jackson C. and Apel J. (ed.). *Synthetic Aperture Radar Marine User's Manual*. U.S. Department of Commerce, Washington DC, USA: National Oceanic and Atmospheric Administration; 2004. pp. 263-275

78 Hühnerfuss, H. 'Basic physicochemical principles of monomolecular sea slicks and crude oil spills' in Gade, M., Hühnerfuss, H., Korenowski, G. M. (ed.). *Marine Surface Films*. Berlin, Germany: Springer-Verlag; 2006. pp.21-35